

DESIGN AND MICROFABRICATION OF ANNULAR CONCENTRIC
CAPACITIVE MICROMACHINED ULTRASONIC TRANCDUCER

A THESIS SUBMITTED TO
THE GRADUATE SCHOOL OF NATURAL AND APPLIED SCIENCES
OF
MIDDLE EAST TECHNICAL UNIVERSITY

BY

PARISA SHARIF

IN PARTIAL FULFILLMENT OF THE REQUIREMENTS
FOR
THE DEGREE OF MASTER OF SCIENCE
IN
MICRO AND NANOTECHNOLOGY PROGRAM

FEBRUARY 2014

Approval of the thesis:

**DESIGN AND MICROFABRICATION OF ANNULAR CONCENTRIC
CAPACITIVE MICROMACHINED ULTRASONIC TRANCDUCER**

Submitted by **PARISA SHARIF** in partial fulfillment of the requirements for the degree of
**Master of Science in Micro and Nanotechnology Department, Middle East Technical
University** by,

Prof. Dr. Canan Özgen _____
Dean, Graduate School of **Natural and Applied Sciences**

Prof. Dr. Tayfun Akın _____
Head of Department, **Micro and Nanotechnology**

Assoc. Prof. Dr. Barış Bayram _____
Supervisor, **Electrical and Electronics Eng. Dept., METU**

Prof. Dr. Raşit Turan _____
Co-Supervisor, **Physics Dept., METU**

Examining Committee Members:

Prof. Dr. Cengiz Beşikçi
_____ Electrical and Electronics Eng. Dept., METU

Assoc. Prof. Dr. Barış Bayram _____
Electrical and Electronics Eng. Dept., METU

Prof. Dr. Hayrettin Köymen _____
Electrical and Electronics Eng. Dept., Bilkent University

Assoc. Prof. Dr. Ali Çırpan _____
Chemistry Dept., METU

Assist. Prof. Dr. Kıvanç Azgın _____
Mechanical Eng. Dept., METU

Date:

07.02.2014

I hereby declare that all information in this document has been obtained and presented in accordance with academic rules and ethical conduct. I also declare that, as required by these rules and conduct, I have fully cited and referenced all material and results that are not original to this work.

Name, Last name: Parisa Sharif

Signature:

ABSTRACT

DESIGN AND MICROFABRICATION OF ANNULAR CONCENTRIC CAPACITIVE MICROMACHINED ULTRASONIC TRANSDUCER

Sharif, Parisa

M. Sc., Department of Micro and Nanotechnology

Supervisor: Assoc. Prof. Dr. Barış Bayram

February 2014, 86 pages

In this thesis, a novel concentric annular CMUT design has been fully designed. All design parameters are determined based on the analytical expressions based on CMUT theory. Each CMUT design consists of 4 concentric disc-shaped elements, having equal membrane areas. Each element features hexagonal CMUT cells having side lengths of 50 μm up to 80 μm . The CMUT design features fully-metallized membranes for robust operation. The novel CMUT design presented in this thesis is a state-of-the-art design based on microfabrication using direct wafer bonding technology. A complete microfabrication process flow has been developed for the realization of the CMUT design. Diamond coating on the silicon wafer has been characterized in terms of residual stress via Raman Spectroscopy measurements, and viability as a membrane material has been shown. . These measurements result in stresses between 385 compressive stresses up to 364 tensile stress regardless of the type of diamond and underlying silicon or silicon dioxide layer. An interlayer of PECVD-SiO₂ is used on the diamond layer. Rapid thermal annealing (RTA) is used to improve the quality of the oxide layer, which is characterized thoroughly using a V-VASE ellipsometer. A surface activation for direct wafer bonding is developed based on a combination of UV/Ozone treatment followed by O₂-plasma-activation

using RIE. A successful bonding is achieved on two flat wafer surfaces. Due to lack of some essential cleanroom capabilities, a fully functional prototype could not be realized in our work. However, it is straightforward to microfabricate the CMUT based on the outcome of this thesis in the presence of a cleanroom having the essential equipment and setup.

ÖZ

DISK SEKİLLİ ESİERKEZLİ KAPASİTİF MİKROURETİLMİS ULTRASONİK CEVİRGECLERİN TASARIMI VE MİKROÜRETİMİ

Parisa, Sharif

M. Sc., Department of Micro and Nanotechnology

Supervisor: Assoc. Prof. Dr. Baris Bayram

February 2014, 86 pages

Bu tezde, özgün disk şekilli eş merkezli CMUT tasarımı tümü ile tasarlanmıştır. CMUT teorisine dayalı analitik denklemler kullanılarak tüm tasarım parametreleri belirlenmiştir. Her CMUT tasarımı 4 eş merkezli disk şekilli eş eleman içermektedir, öyleki eleman alanları birbirine eşittir. Tüm elemanlar altıgen şekilli ve kenar uzunluğu 50 μm 'den 80 μm 'ye kadar olan CMUT hücreleri içermektedir. Güvenilir çalışma için tamamıyla metal kaplı membranlar bu CMUT tasarımında kullanılmıştır. Bu tezde sunulan CMUT tasarımı doğrudan pulların birleştirilmesi metoduna dayalı son yenilikleri içermektedir. Bu CMUT tasarımının gerçekleştirilmesine yönelik tüm mikroüretim süreci geliştirilmiştir. Silikon pul üzerindeki elmas kaplama Raman spektroskopisi metoduyla gerilim yönünden değerlendirilmiş ve membrane malzemesi olarak uygunluğu gösterilmiştir. Bu ölçümler vesilesile elmasın temel silikon ya da silikon dioksit tabakasından bağımsız olarak, 364 MPa bir çekme gerilimden 385 MPa sıkıştırma gerilime kadar sonuçlanmıştır. PECVD-SiO₂ ara katmanı elmas kaplama üzerinde kullanılmıştır. Hızlı ısı işlem (RTA) kullanılarak oksit tabakanın kalitesi artırılmış ve V-VASE ölçümleriyle bu kalite incelenmiştir. UV/ozon temizliği ile sonrasında uygulanan RIE yolu O₂-plazma-aktivasyonu kullanılarak doğrudan pulların birleştirilmesi metoduna uygun yüzey aktivasyonu gerçekleştirilmiştir. İki düz pul yüzeyi arasında başarılı bağ elde edilmiştir. Bazı gerekli temizalan kabiliyetlerinin eksikliğinden

dolayı, tümüyle çalışır prototip bu çalışmada gerçekleştirilememiştir. Fakat, bu tezin katkılarıyla CMUT üretiminin uygun cihaz ve imkanların olduğu bir temizalanda gerçekleştirilmesi mümkündür.

To my parents, and dear brother

ACKNOWLEDGEMENTS

This work is in part supported by the Scientific and Technological Research Council of Turkey (TUBITAK), under grant number of 1110E099. TÜBA-GEBİP and METU-BAP-03-02-2013-001 project supports are acknowledged.

All microfabrication work is carried out in UNAM National Nanotechnology Research Center in Bilkent University, and I would like to thank the former president Prof. Dr. Salim Ciraci, and the acting president Assoc.Prof.Dr. Mehmet Bayindir for supporting our project work.

I would like to give my best thanks to my thesis Supervisor Assoc. Prof. Dr. Baris Bayram for all his financial support and guidance during this project.

I would like to thank Assist. Prof. Dr. Alpan Bek for his guidance and friendly attitude during the discussions and measurements that we had for stress measurement via Raman spectroscopy.

I would also like to present my thanks to Semih Yasar for his cleanroom equipment trainings and his support throughout our work in the UNAM cleanroom.

I would also like to express my special thanks to Sedat Dogru for his support, sharing his knowledge, and his help in mask designing.

I would also express my gratitude to Mohammad Maadi and Isik Can in ULTRAMEMS Research Group who helped me a lot to continue with this project by providing a nice research environment.

I would also thanks to my friends in Middle East Technical University, Mona Zolfaghari, Negin Bagherzadi, Nasim Seyedpour and Nardin Avishan who helped me a lot to have a friendly atmosphere during this study.

In the end, I would like to give my special thanks to my kind father Dr. Rahim Sharif, my lovely mother Parvin Azizian, my dear uncle Prof. Dr. Ali Sharif and my dear brother Pouria Sharif who helped me emotionally during my life and studies in METU.

TABLE OF CONTENTS

ABSTRACT	v
ÖZ	vii
ACKNOWLEDGMENTS	x
TABLE OF CONTENTS	xi
LIST OF FIGURES	xv
LIST OF TABLES	xvii
CHAPTERS	
1. INTRODUCTION	1
1.1 Micro-Electro-Mechanical Systems (MEMS)	1
1.2 Ultrasound measurement system	2
1.3 Piezo Transducer	3
1.4 Micromachined Ultrasound Transducers (MUTs)	3
1.5 Capacitive Micromachined Ultrasonic Transducers (CMUTs).....	4
1.6 Objectives of the Thesis	6
2. HISTORY AND THEORY OF CMUTs	7
2.1 Brief history of CMUTs	7
2.1.1 Technology of analysis of CMUTs	7
2.1.2 Technology of CMUT Microfabrication and Prototypes	11
2.1.3 Developed Microfabrication Techniques	13
2.1.4 Diamond as a Membrane Material	14

2.2 CMUTs Theory	14
2.2.1 Collapse Voltage	15
2.2.2 Snap-back Voltage	16
2.2.3 Electromechanical Coupling Coefficient	17
2.2.4 Resonance Frequency.....	17
2.2.5 Electrical Equivalent Circuit of CMUT	18
2.3 Further CMUTs.....	19
2.4 Application Areas of CMUTs	19
2.4.1 Air Application	19
2.4.2 Immersion Application.....	20
3. ANNULAR CMUT DESIGN	21
3.1 Disk CMUT Mask Designing	22
3.2 Disk CMUT Mask with 50 μm hexagon cells	25
3.2.1 Steps of drawing 1st mask: CAVITY	25
3.2.2 Steps of drawing 2nd mask: TOPLAYER	28
3.2.3 Steps of drawing 3rd mask: METAL	30
3.3 Disk CMUT mask with 60 μm hexagon cells	31
3.3.1 Steps of drawing 1st mask: CAVITY	31
3.3.2 Steps of drawing 2nd mask: TOPLAYER	33
3.3.3 Steps of drawing 3rd mask: METAL	34
3.4 Disk CMUT mask with 70 μm hexagon cells	36
3.4.1 Steps of drawing 1st mask: CAVITY	36

3.4.2	Steps of drawing 2nd mask: TOPLAYER	37
3.4.3	Steps of drawing 3rd mask: METAL	38
3.5	Disk CMUT mask with 80 μm hexagon cell	40
3.5.1	Steps of drawing 1st mask: METAL	40
3.5.2	Steps of drawing 2nd mask: TOPLAYER	41
3.5.3	Steps of drawing 3rd mask: TOPLAYER	42
4	DIAMOND MEMBRANE CHARACTERIZATION FOR CMUT's.....	45
4.1	Diamond as a Membrane Material	45
4.2	Stress Measurements Techniques	46
4.3	Raman spectroscopy	47
4.4	Raman Measurement Results.....	48
4.4.1	UNDOPED MCD	48
4.4.2	DOPED MCD.....	49
4.4.3	UNDOPED NCD.....	50
4.4.4	DOPED NCD	51
4.4.5	UNDOPED UNCD.....	52
4.4.6	DOPED UNCD	54
4.5	Conclusion	56
5	MICROFABRICATION of DIAMOND-BASED CMUT.....	57
5.1	CAVITY Patterning	57
5.1.1	Photolithography of Silicon Wafer	57
5.1.2	Wet and Dry Etching on Cavity Definition.....	58

5.1.3 UV Cleaning System	60
5.2 SiO ₂ Deposition and CMP of Diamond Wafer for Wafer bonding	60
5.3 Wafer Bonding	62
5.3.1 RCA Cleaning	62
5.3.2 Surface Wettability	63
5.3.3 Wafer Bonding and High Temperature Annealing	63
5.4 Etching the Top Wafer	64
5.5 MASK 2: TOPLAYER.....	67
5.6 MASK 3: METAL.....	67
5.7 Overview of Microfabrication steps of CMUTs with Diamond Membranes	68
6 CONCLUSIONS AND FUTURE WORKS	79
REFERENCES	81

LIST OF FIGURES

FIGURES

Figure 1.1 the membrane of a MUT [4]	4
Figure 1.2 A cross section view of a basic CMUT cell [5]	5
Figure 2.1 First order lumped electro-mechanical model of a CMUT element [9] ...	8
Figure 2.2 Collapse operation regime of CMUT [12]	9
Figure 2.3 Lumped Electro Mechanical of a CMUT	15
Figure 2.4 Electrical Equivalent Circuit of CMUT [9]	17
Figure 3.1 Inner and Outer Circles of a Hexagonal Membrane	21
Figure 3.2 Mask Plate	23
Figure 3.3 Alignment	23
Figure 3.4 CMUT disk mask with hexagon cells	24
Figure 3.5 the property window of Macro	25
Figure 3.6 CAVITY mask with 50 μ m hexagon cells.....	27
Figure 3.7 CAVITY mask with 50 μ m hexagons (central view, x5 lens)	27
Figure 3.8 Tori.....	28
Figure 3.9 TOPLAYER Mask for 50 μ m hexagonal cells	29
Figure 3.10 METAL Mask for 50 μ m hexagonal cells	31
Figure 3.11 1CAVITY mask with 60 μ m hexagon cells.....	32
Figure 3.12 TOPLAYER Mask for 60 μ m hexagon cells	33
Figure 3.13 METAL Mask for 60 μ m hexagon cells	35
Figure 3.14 CMUT disk mask with 60 μ m hexagon cells.....	35
Figure 3.15 CAVITY mask with 70 μ m hexagon cells	36

Figure 3.16 TOPLAYER Mask for 70 μ m hexagon cells	37
Figure 3.17 METAL Mask for 70 μ m hexagon cells	38
Figure 3.18 CMUT disk mask with 70 μ m hexagon cells	39
Figure 3.19 CAVITY mas with 80 μ m hexagon cells	40
Figure 3.20 TOPLAYER Mask for 80 μ m hexagon cells	41
Figure 3.21 METAL Mask for 80 μ m hexagon cells	42
Figure 3.22 CMUT disk mask with 80 μ m hexagon cells	43
Figure 4.1 Diagram of Raman peak	47
Figure 4.2 Spectrum of UNDOPED MCD	49
Figure 4.3 Spectrum of DOPED MCD	50
Figure 4.4 Spectrum of UNDOPED NCD.....	51
Figure 4.5 Spectrum of DOPED NCD.....	52
Figure 4.6 Spectrum of UNDOPED UNCD	53
Figure 4.7 Spectrum of UNDOPED UNCD with 0.3 μ m thickness	53
Figure 4.8 Spectrum of DOPED NCD.....	54
Figure 4.9 Spectrum of UNDOPED UNCD with 0.3 μ m thickness	55
Figure 5.1 (a) spinners, (b) hotplates	58
Figure 5.2 Cavity Patterned Wafer during developing	58
Figure 5.3 PIRHANA cleaning.....	59
Figure 5.4 Microscope image of cavity pattern with 80 μ m hexagons (Central view, x20 lens)	59
Figure 5.5 UV cleaning system	60
Figure 5.6 (a) ‘n’ and ‘k’ constants graphics before RTA (b) ‘n’ and ‘k’ constants graphics after RTA.....	61

Figure 5.7 RCA cleaning system	62
Figure 5.8 Wafer bonding annealing system	63
Figure 5.9 Wafer Bonding Results	64
Figure 5.10 Wafer holder with backside and edge protection	64
Figure 5.11 TMAH process setup	65
Figure 5.12 Microscope images of surface of wafer after TMAH process	66
Figure 5.13 Process steps 1 to 2, Step 1: n-type silicon wafer with SiO ₂ Layer, Step 2: Covering the wafer with photoresist	68
Figure 5.14 Process steps 3 to 4, Step 3: Photoresist patterning with cavity mask, Step 4: SiO ₂ etching with RIE	69
Figure 5.15 Process steps 5 to 7, Step 5: Photoresist stripping with O ₂ plasma, Step 6: Silicon wafer with diamond layer, Step 7: SiO ₂ Deposition with PECVD	70
Figure 5.16 Process steps 8 to 9, Step 8: Satisfy the surface roughness of PECVD-SiO ₂ with CMP, Step 9: Direct bonding of wafers at 450°C	71
Figure 5.17 Process steps 10 to 11, Step 10: Total TMAH etching of 525 μm silicon layer of top wafer, Step 11: PECVD SiO ₂ covering of diamond surface	72
Figure 5.18 Process steps 12 to 13, Step 12: Photoresist covering, Step 13: Photoresist patterning with TOPLAYER mask.....	73
Figure 5.19 Process steps 14 to 15, Step 14: SiO ₂ etching with RIE, Step 15: Diamond etching with RIE and photoresist stripping	74
Figure 5.20 Process steps 16 to 17, Step 16: SiO ₂ etching with RIE, Step 17: Metallization.....	75
Figure 5.21 Process steps 18 to 19, Step 18: Photoresist Covering, Step 19: Patterning Photoresist with Metal Mask	76
Figure 5.22 Process Step 20: Metal etch with chemicals and photoresist stripping with O ₂ plasma	77

LIST OF TABLES

TABLES

Table 3.1 CMUT Design Parameters.....	22
Table 3.2 Macro inputs for CAVITY mask with 50 μm hexagonal cells.	26
Table 3.3 TOPLAYER Mask Properties with 50 μm hexagonal cells	29
Table 3.4 METAL Mask Properties with 50 μm hexagonal cells	30
Table 3.5 Inputs of Macro for CAVITY mask with 60 μm hexagonal cells	32
Table 3.6 TOPLAYER Mask Properties with 60 μm hexagonal cells	33
Table 3.7 METAL Mask Properties with 60 μm hexagonal cells	34
Table 3.8 Inputs of Macro for CAVITY MASK with 70 μm hexagonal cells	36
Table 3.9 TOPLAYER Mask Properties for 70 μm hexagon cells	37
Table 3.10 METAL Mask Properties for 70 μm hexagon cells	38
Table 3.11 Inputs of Macro for CAVITY mask with 80 μm hexagonal cells	40
Table 3.12 TOPLAYER Mask Properties for 80 μm hexagon cells	41
Table 3.13 Metal Mask Properties for 80 μm hexagon cells	42
Table 4.1 Stress Measurement Techniques.....	46
Table 4.2 Properties of MCD, NCD and UNCD	48
Table 4.3 UNDOPED MCD PROPERTIES	49
Table 4.4 DOPED MCD PROPERTIES	50
Table 4.5 Properties of UNDOPED NCD	51
Table 4.6 Properties of DOPED NCD	52
Table 4.7 Properties of UNDOPED UNCD	54

Table 4.8 Properties of DOPED UNCD.....	56
Table 4.9 Properties of all diamond wafers	57
Table 5.1 Fireplace glass properties	63
Table 5.2 (100) etch rates according to temperature	65

CHAPTER 1

INTRODUCTION

1.1 Micro-Electro-Mechanical Systems (MEMS)

Recently an outstanding trend that is known as MEMS attracts many researchers attention. MEMS (Micro Electro Mechanical Systems) refer to electro-mechanical elements and miniaturized mechanical devices and structures constructing by different techniques of micro fabrication. The range that is defined for the scale and dimensions of MEMS devices is from one micron to some millimeters. Simple structures without any moving parts, to very complex tools with multiple moving parts those are controlled by integrated microelectronics, various can be considered in MEMS category. The dominant objective of MEMS is to offer some kind of mechanical functionality for elements without considering their movement. Micro-scaled structures, actuators, sensors, and microelectronics, can be considered as interesting and important elements in MEMS which are known as microsensors and microactuators. Transducers those are used for conversion of one form of energy to another form can contain microactuators and microsensors; as an illustration, the important usage of microsensors, is conversion of a measured mechanical signal into an electrical signal.

During the past decades, various microsensors are offered for different kinds of sensing modality such as pressure, temperature, magnetic fields, inertial forces, radiation, chemical species, etc. considerably, most of these micromachined sensors those are proposed in recent research works, in comparison with their macroscale counterpart have better and enhanced performances. For instance, the micromachined version of an ultrasound transducer, mostly have a better performance in comparison with the macroscale fabricated ultrasound transducers. Beside the better performance of MEMS devices which is discussed above and many other benefits, method of batchfabrication production which is, for example, used in integrated circuit industry can reduce the cost of production [1].

This thesis will report design and fabrication of new ultrasound transducers for ultrasound therapeutic applications. This chapter gives an introduction on the CMUTs. Section 1.2 continues this chapter by providing an overview around the ultrasound transducers.

1.2 Ultrasound measurement system

Ultrasound measurement systems operate by using of sound waves and the reflection of them. These systems can used for testing an object without doing any operation on it or taking it apart. Scattering or reflection of the radiated sound waves can happen whenever they face obstacles or in homogeneities of an object. In these devices, there is a measurement probe which is hit by reflected waves with diverse time delays. According to the particular sound distance and speed mentioned delays can be evaluated, and presented as an image.

Sound waves over the audible range (about 20 Hz to 20 kHz) can describe the term ultrasound. Good image resolution that can be provided by narrow beam and a short pulse is result of high frequency. Anyhow, attenuation will be increased with the rising of the frequency. Ultrasound waves of the range (2-10 MHz) are useful in medical applications. In some special cases frequencies up to 40 MHz can be applied [2]. Equation 1.1, declares the relation between frequency and wavelength.

$$\lambda = \frac{c}{f} \quad (1.1)$$

In the equation, c is the speed of sound in the medium which should be probed. The wavelength λ is proportional to the inverse amount of frequency f . As it is shown in the equation 1.1, the utilization of the ultrasonic transducers is trade off. Due to the fact that attenuation will be increased with the rising of the frequency, A transducer that act in high frequencies would have a wave propagation which is supported from attenuation therefore, cannot be able to interpenetrate inside the object. It should be considered that in the range of high frequencies, the resolution of the transducer will increase. So, this tradeoff is crucial parameter in ultrasound transducer design. There are lots of applications those use ultrasound measurement systems. According to the system utilization, various frequencies and intensities can be applied.

The ultrasound measurement system made from several elements. The ultrasonic transducer is a small but very crucial part of the system. The role of transducer is emitting and receiving the acoustic signal. Electronics provide the signal manipulation and interpretation. Nowadays, the array of transducers is applied to create an image instead of the single element. This method is famous due to the fact that array of transducers can be controlled electronically in order to be eligible to scan in variety

of directions for obtaining an image. At last, the computed signal can provide the final images.

In this thesis, the main objective is to design a modern transducer. Ultrasonic transducers can be categorized on account of their physical mechanism upon which they are based to convert electrical energy into ultrasonic energy, and vice versa. Magnetostriction, piezoelectricity and electrostatics are some of the physical mechanisms that used to emit and receive ultrasound. Historically, piezoelectric crystals, ceramics, polymers and recently piezocomposite materials have been used to emit and receive ultrasound. However, the concept of electrostatic transducers is as old as the primary piezoelectric transducers, piezoelectric materials have dominated ultrasonic transducer technology

1.3 Piezo Transducer

The term piezo is derivation of the term pressure in Greek. Jacques and Pierre Curie, in 1880, discovered with the application of the pressure to a quartz crystal, electric potential could be generated. Later, this phenomenon considered as piezoelectric effect. There is also an inverse piezoelectric effect that is observed when the shape of a piezoelectric material would be changed by exposing them, to electric potential; this inverse piezo effect is used in actuators while, the piezo effect is applicable for sensors. The simulation of a capacitor can be done by piezo ceramic plates using in transducers. The ceramic acts as a dielectric among its metalized electrodes. A homogeneous lateral contraction can be generated by the electric field by applying voltage; in this contraction, the direction of this electric field is perpendicular to the direction ceramic plate which is denominated as transverse piezoelectric effect. The major point for controlling the transducer modules is offered by the magnitude of the lateral contraction which is defined by the electric field strength. Similar to conventional actuators, the force transmission is done by the modules attaching to the surface.

The piezo ceramic replies so fast to change of the electric field. The generation of vibrations in the range of kilohertz can be done. Various excitation voltages and diverse contraction amounts could be possible by considering the ceramic dimensions and its type. [3]

1.4 Micromachined Ultrasound Transducers (MUTs)

Emitting and receiving the acoustic waves can be done by a kind of electronic devices that are known as ultrasonic transducers. Common piezo-electric transducers cannot

consider as a useful transducer in case of converting of electric to acoustic energy. In the air atmosphere, the operating frequencies of these devices are low while, the immersed transducers operate in high frequencies. For instance, Ginzton Lab productions of MUTs which are based on micromachining technology work at very high frequencies in the air atmosphere and operate efficiently. By benefitting the micromachining approach in MUTs industrial, fabrication of large arrays of them is possible which result is in low cost.

A MUT is mainly created from two electrodes: a silicon bulk and silicon nitride membrane vibrating on top of it (Figure 1.1); this vibration is because of applying an AC signal across these two electrodes. This vibration can be characterized by the resonant frequency which is result of radius of the stretched membranes and residual stress [4].

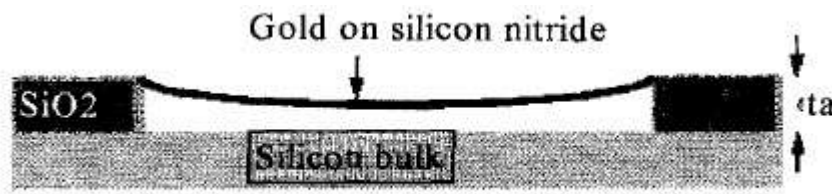


Figure 1.1 the membrane of a MUT [4].

When a voltage is applied between the membrane and the substrate, the electrostatic forces led to the membrane collapse on substrate. The generation of an ultra sound wave, occur when the AC signal is applied to the top electrode. In the other hand, if ultrasound wave is applied across the biased membrane, it will generate an AC voltage. Micromachining is considered as a useful method for the fabrication of ultrasound transducers, due to the fact of existence of micro-scaled elements.

1.5 Capacitive Micromachined Ultrasonic Transducers (CMUTs)

The term CMUT which is capacitive micromachined ultrasonic transducer is a new concept in the ultrasonic transducers field. The commercial versions of ultrasonic transducers are mostly working based on piezoelectricity. CMUTs have many advantages: large arrays of CMUTS can be fabricated easily, a wider bandwidth and bonding with the integrated circuits. The operation of CMUT is because of capacitive structure. In this capacitive structure, the electrostatic forces are generated among two electrodes which are separated from each other with a very tiny gap. These electrostatic forces, are used to emit and receive ultrasound waves.

As it is shown in figure 1.2, a cross section of the basic CMUT structure can be observed which was produced at Stanford University in 1994 [4]. Two years later, a new kind of CMUT which had an operating frequency above 10 MHz was invented. Micromachining techniques were used for fabrication of CMUTs. In a silicon wafer, a cavity is formed, and a thin layer which is suspended on the top of it. This thin layer which acts as metalized layer membrane, and the silicon substrate, together can be considered as a capacitance electrodes.

As it was mentioned before, CMUTs will work as a transmitter of ultrasound of an AC signal is applied between the biased electrodes. From another point of view, CMUTs will work as a receiver of ultrasonic waves, if ultrasound waves are applied across the biased membrane.

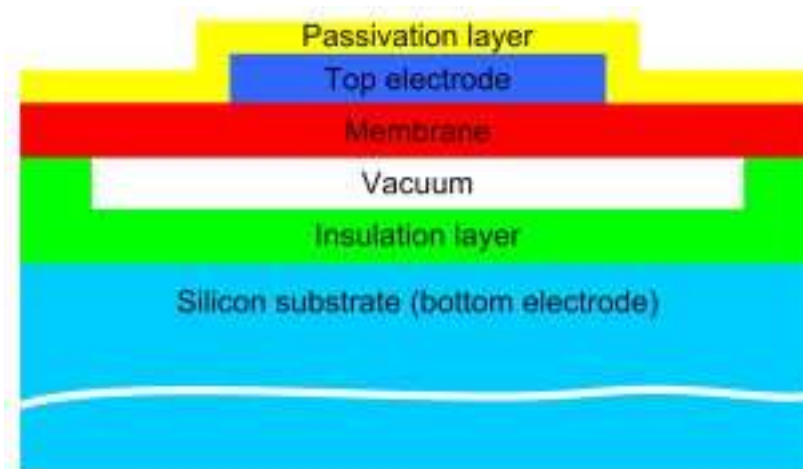


Figure 1.2 a cross section view of a basic CMUT cell [5].

By the usage of common integrated circuit (IC) fabrication processes, a capacitor cell contains top electrode suspended above bottom electrode which is heavily doped silicon. For the prevention of shorting of two electrodes in case of contact, and insulating layer is localized. Several kind of array shape could be possible, by optimization of elements of transducer in case of various geometries. A single transducer element contains a lot of small capacitor cells those are connected in a parallel format.

1.6 Objectives of the Thesis

The objective of the thesis is to design and microfabricate a novel concentric annular CMUT design. Based on this objective, all design parameters are to be determined based on the analytical expressions of CMUT theory.

A microfabrication process flow is to be developed and realized using direct wafer bonding technology. A complete microfabrication process flow is to be developed for the realization

of the CMUT design. Using the available resources, on a best effort basis, realization of the proposed CMUT design is planned during the course of the thesis.

Viability of diamond as a membrane material is to be investigated using Raman Spectroscopy, and residual stress measurement is to be performed.

Direct wafer bonding method is to be developed using a special activation based on UV-Ozone and plasma activation.

CHAPTER 2

HISTORY AND THEORY OF CMUTs

2.1 Brief history of CMUTs

The study which was done by B. T. Khuri-Yakub and Haller in 1993, a capacitive micromachined ultrasonic transducer (CMUT) with more improved technology of fabrication and enhanced performance [6]. This kind of ultrasonic transducer which worked at very high frequencies around 11 MHz and in air can be compatible with alternative piezoelectric transducers. In the fabrication of this transducer, silicon nitride membranes were designed in a circular form which a metalized electrode suspended on top of it in order to be vibrated by applied voltages [7]. At 4, 6, and 8 MHz with a 48 dB signal to noise ratio, these devices worked. From 1 up to 20 MHz, the transmission was reported.

It was in 1998, that the dominant enhancement in the performance of CMUT was observed [8]. This work can be considered as pioneer research in CMUT study, because of offering the Air-coupled through-transmission of steel and glass at 2.3 MHz for the first time. CMUTs were observed to work in water, with a dynamic range of 60 dB that was measured at from 1 to 20 MHz. It was reported that immersed CMUTs would be able to reach the 110 dB dynamic range of the air CMUTs.

2.1.1 Technology of analysis of CMUTs

Several measurement techniques were done on CMUTs in order to analysis them. To scale the ultrasonic efficiency of the device, three different measurement systems were used [6]. The first system was an impedance analyzer which was used to measure the input electrical impedance of the device under 40 V bias voltages. Great accord between measurement and theory was found when the measured data were compared with theory.

A common pitch-catch system was used to measure the change in the current through the device using a high input impedance amplifier. Ultrasonic waves were emitted and received by two identical CMUTs. The signal was detected by biasing the receive transducer with a 100-V bias.

The third system was used to measure the performance of the CMUT was an optical interferometer to measure the displacement of the membrane. This system was able to detect the subangstrom displacements.

First order analysis, lumped electro-mechanical model of a CMUT element was reported in 1998 [9]. It was assumed that a lumped electro-mechanical model consisting of a linear spring, a mass and a capacitor as shown in figure 2.1. Mechanical impedance of membrane was calculated and spring softening effect, collapse and snap-back formations of membrane were also calculated [9].

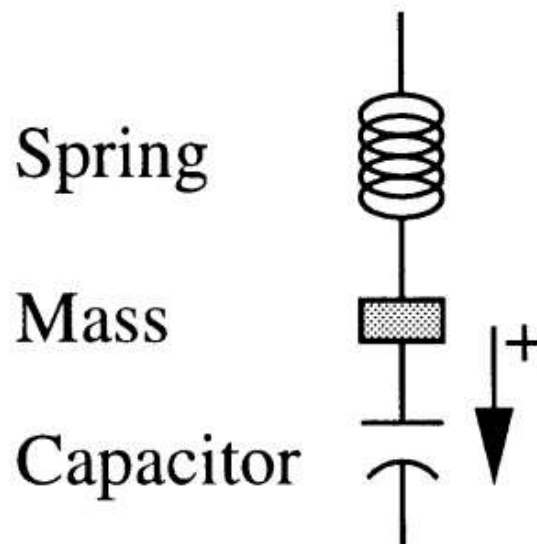


Figure 2.1 First order lumped electro-mechanical model of a CMUT element [9].

The equivalent circuit model of the CMUT was not contained important characteristics such as coupling to the substrate and the ability to obtain the effect of cross-talk between elements of an array of CMUT [10]. To overcome these lacks, a finite element analysis of the CMUT were done using the commercial code ANSYS. Cross-talk effect was happened between elements of an array of transducer because of to two main sources: coupling through a Stoneley wave propagating at the transducer-water interface and coupling through Lamb waves propagating in the substrate. In order to reduce the cross-talk effect, some structural variations of the substrate were checked, which included decreasing of its thickness and creating etched trenches or polymer walls between array elements [10].

The electromechanical coupling coefficient is a crucial figure of merit of CMUTs. The transducer bandwidth is determined by the electromechanical coupling efficiency. The coupling coefficient is the ratio of delivered mechanical energy to the stored total energy in the transducer. The calculation and measurement of coupling coefficient for CMUTs was presented by using the finite element method for calculations [11]. The analysis showed that, this coefficient is not affected by series and parallel parasitic capacitances of the device and another important detail that was indicated during the analysis was radius of electrode which was set to the half of the membrane radius was an optimal value for collapse voltage value. Any increase in electrode radius dose not affect collapse voltage, the only thing that will be affected it is parasitic capacitances. Besides, it is possible to have a device without collapse by adjusting the series capacitances [11].

New operation regimes for CMUTs were reported in 2003 [12]. Traditionally, CMUTs were excited at a bias voltage lower than the collapse voltage. In the reported new operation regime, first the CMUT was biased with voltage higher than collapse voltage. Second, the bias voltage applied to the collapsed membrane was reduced between the collapse and snapback levels without releasing the membrane. Finally, the CMUT is excited with an ac signal at the DC voltage bias point while keeping total voltage between the collapse and snapback voltages [12]. In this mode, the center of the membrane is always in contact with the substrate as shown in figure 2.2.

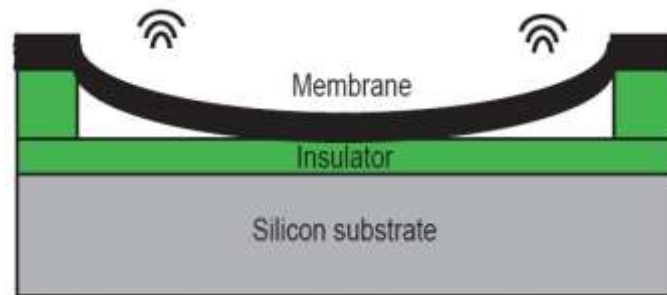


Figure 2.2 Collapse operation regime of CMUT [12].

Finite element method analysis results showed that a CMUT operating in this new regime, have a coupling efficiency higher than a CMUT operating in the conventional regime [12].

Wide acoustic wave devices have been built using the excitation of Lamb waves as a transducer. Most of these devices operate with using an interdigital electrode configuration at the surface of piezoelectric ceramics. A new Lamb wave device was Built by using CMUTs in 2003 [13]. In this structure rectangular membrane was used

to excite and receive Lamb waves from silicon substrate. A new CMUT equivalent circuit was designed for rectangular membranes. The device was operated in 2.1 MHz [13].

High power transmission regime of CMUTs was designed to achieve maximum efficiency [14]. The conventional modes of the CMUTs need a bias voltage around the collapse voltage. Total acoustic output pressure is limited by the efficiency of the CMUT. This design was proposed to the collapse-snapback operation of the CMUT. The membrane was collapsed onto the substrate in the collapsing cycle, and released in the snapback cycle. The collapse-snapback mode dominates the restrictions of the conventional operation. In this operation a larger range of membrane deflection profiles for both collapsed and released profiles, were used to generate higher acoustic output pressures. If appropriate bias condition used in the collapse-snapback operation, it can be allowed the application of pulse voltages larger than the difference of collapse and snapback voltages [14].

DC bias below collapse voltage operation scheme that used for electrostatic transducers was borrowed for CMUTs. In this situation, the CMUT membrane deflects to the substrate, so that in the both receive and transmit mode the center of membrane is free to move. In this CMUT, hexagonal membranes were used in order to increase the active area [15].

Experimental characterization of collapse-mode operation of CMUTs were reported and compared with conventional mode in 2006. CMUTs are conventionally operated by applying a direct current (DC) bias voltage less than the collapse voltage of the membrane, so that the membrane is deflected toward the bottom electrode. In CMUTs conventional operation mode, there is not any contact between the membrane and the substrate because by applying DC bias voltage less than the collapse voltage of the membrane, the membrane is deflected toward the substrate so that the maximum AC displacement occurs at the center of the membrane but in collapse-mode operation of CMUT, the center of the membrane is always in contact with the substrate so the maximum AC displacement occurs along the ring formed between the center and the edge of the membrane. The impedance measurements in air with impedance analyzer, pulse-echo experiments in immersion (oil medium), and optical displacement measurements in immersion with laser interferometer for both conventional and collapse-mode operations were done. Frequency response and efficiency of the transducer in conventional and collapse modes were compared and it was shown a membrane in collapsed mode can be emit and receive ultrasound more efficiently than a membrane operated in the conventional mode. In addition, the center frequency of a CMUT that operated in collapsed mode can be changed by varying the applied DC bias voltage [16].

As mentioned before crosstalk is the coupling of energy between the elements of a CMUT array. This effect reduces the performance of CMUT in applications such as medical imaging and high intensity focused ultrasound treatment (HIFU) in medicine. Experimental, analytical, and finite element methods were performed using 1-D CMUT array to determine the causes and effects of crosstalk in CMUTs. The FEM analysis was considered conventional and collapse mode operations. It was shown the crosstalk effect in collapse mode is lower than conventional mode operation because in collapse mode shifting of center frequency to higher values decreases the crosstalk. Besides, it was shown coating of the PDMS on CMUT elements did not significantly reduction affect on the crosstalk level, but decreased the phase velocity for both operation modes [17].

For increasing the total output pressure of CMUTs, the fill factor is an important factor. This factor also affects the sensitivity of the receiver of transducers. Rectangular shape CMUT membranes with low cell-to-cell spacing and high aspect ratio to achieve high fill factor were reported in 2007. In other hand, it was shown that rectangular membranes could have better fill factor but it was not suitable for operation in air, under continuous wave (CW) due to the emission of low output pressures [18].

As mentioned before with optimizing the membrane shape and its geometry the performance of CMUT can be improved. In order to achieving this goal piston shape membranes were reported to improve device performance in terms of transmission efficiency, reception sensitivity, and fractional bandwidth (FBW) [19].

A comprehensive comparison between a collapse-mode and a conventional-mode of CMUT was reported in 2013 [20]. Finite element analysis (FEA) results showed that the collapse-mode CMUT has higher output pressure sensitivity (46.5 KPa/V) than the conventional CMUT (13.1 KPa/V), and achieves a 3-dB fractional bandwidth (FBW) of 124% compared with 128% for the conventional mode.

2.1.2 Technology of CMUT Microfabrication and Prototypes

The fabrication of a CMUT has been developed during last decade. The size and shape of the CMUT cells, the membrane material and the thickness of membrane has been modified over years to achieve different goals. There are several alternative techniques to fabricate a working CMUT. The main principle of emitting the ultrasound and receiving of the reflected wave is basically the same. Most of the techniques are familiar micromachining methods. There is however two general methods outlined.

The first method is named the sacrificial release process, which is a surface micromachining process. This method is still widely used in CMUT microfabrication. In surface micromachining the transducers are fabricated by use of thin-film depositions, thin-film etching and photolithography on top of a wafer substrate, it means all the process steps are done on the surface of substrate. The substrate operates as a bottom electrode, and in general is a low-resistivity silicon wafer. In order to reaching high conductivity the silicon wafer is heavily doped. The substrate conductivity is one of the most crucial parameters, because it forms the back electrode. Then on top of the substrate, a thin layer of LPCVD silicon nitride is deposited in order to an etch stop for the following sacrificial layer etching. The next step is depositing polysilicon as a sacrificial layer in order to create the cavity. The membrane is created by depositing a second layer of Si₃N₄ on top of the sacrificial layer. The sacrificial layer is wet etched to release the membrane, then the gap is sealed by deposition of a third layer of LPCVD Si₃N₄ which coats all the surfaces, the cavity is vacuum sealed, and then aluminum is deposited on the wafer as the top electrode of the membrane and the connection pads. One of them is connected to the membrane surface and the other is connected to the substrate. The last step is to cover the metal electrodes with an electrically insulating layer (LTO) in order to wire bonding. The wire bonds and pads are then covered with epoxy to ensure electrical passivation in conducting fluids, and to avoid corrosion [21].

Some improvements and variation were also reported for sacrificial release technique [22]. Generally in CMUTs, silicon wafers has been used as a substrate material but another material like quartz can be used as a substrate. But there is a limitation with using quartz as a substrate because of insulating characteristic of it. In order to serve the quartz substrate as the back electrode of the CMUT should be coated it with a conductive material and this conductive material should be chosen appropriate with process condition.

In sacrificial release method as a sacrificial layer, polysilicon is used. Polysilicon has high compressive stress, and this stress can be damage the large membrane in order to decrease this damage Phospho-silicide-glass was deposited between the polysilicon and silicon nitride to support the membranes [22].

Membrane stiction is the most important problems of sacrificial release technique. After sacrificial layer etching, some water remains inside cavities and channels and causes capillary force of surface pulls the membrane toward the substrate. For solving this problem, the thickness of the membrane should be obtained in order to have higher mechanical restoring force than capillary force. However, controlling the membrane thickness is a critical problem in wet etching process. The membrane material needs to be chosen appropriate the etch rate selectivity of the etchant [22].

As mentioned above, the first method had some limitations on design and manufacturing of CMUTs. The second method that was brought to avoid these limitations is the wafer bonding technique [23]. In this technique two wafers are used to fabricate the CMUT. On the first wafer that is used as a substrate, the cavity structures are fabricated. The second wafer which will become the membrane is brought to bond to the substrate in vacuum condition after a heat treatment. After bonding step, by backside etching of the second wafer, what remains is a series of cavities with membranes stretched above. Finally, the aluminum top electrodes are deposited and patterned on top of the membranes. Wafer bonding is considered better reliability and design flexibility of making CMUTs.

This method obtained some advantages over sacrificial release method. Firstly, membrane and cavity have separated formation and are independent of structure and shape. The optimizing the shape and size of cavity is possible independent of membrane structure. Secondly, wafer bonding method allows changing membrane material independent of cavity style. Lastly, wafer-bonded CMUTs have higher fill factor in contrast to conventional CMUTs. In wafer bonding method, there are no holes and channels etching, that causes increasing the active area. The wafer bonding method process reduces the complexity of CMUT fabrication. The number of lithography masks is reduced and processing time is reduced substantially. The wafer-bonding technique also adds many design flexibilities that improve device efficiency [23].

2.1.3 Developed Microfabrication Techniques

As mentioned before, the fabrication of CMUTs has been developed over years. Cell size controlling was done in order to achieve better sensitivity and dynamic range. Variation of cell size due to timed oxide etching was a crucial problem in conventional CMUTs. Besides, amorphous silicon was used as a sacrificial layer rather than thermal oxide in order to achieve better etching selectivity against the nitride membrane [24].

Different membrane structures was investigated and characterized with different parameters such as membrane formation, vacuum sealing, and electrode metallization [25]. Three sacrificial release CMUT membrane structures were considered: a nitride membrane with an oxide sacrificial layer; a polysilicon membrane with an oxide sacrificial layer; and a nitride membrane with a polysilicon sacrificial layer. According to the theoretical results the polysilicon membrane had the best operation but nitride membranes showed better controllability during the microfabrication process.

Advanced CMUT microfabrication technology allowed to 2-D large arrays to be used for 3-D real-time imaging [26]. It was a big obstacle stand in the way of developing

two dimension ultrasonic-photoacoustic imaging system. CMUT manufacturing advantages could provide a solution for this problem.

In order to use CMUTs in medical application, a biocompatible material must coat the device to using device in contact with the living tissues. PDMS coated CMUTs were reported and characterized [27]. In the fabrication of this device wafer bonding method was used with deposition of biocompatible material step.

To improve reliability issues of a CMUT, isolation post technique instead of full-coverage insulation was reported. This technique was used to eliminate the dielectric charging problem in CMUTs [28].

The electrical breakdown and parasitic capacitance are the crucial parameters that affect the CMUTs operation. In order to eliminate these problems new improvements in CMUT fabrication are reported. The improvements were based on local oxidation of silicon (LOCOS), and on direct wafer bonding [29].

2.1.4 Diamond as a Membrane Material

As mentioned before, wafer bonding approaches makes possible to use different materials as membrane in CMUT structure. For the first time a diamond-based circular CMUT was reported [30]. Diamond is a dominant membrane material for CMUTs. Hardness, high thermal conductivity, high electrical resistivity, transparency, low friction and thermal expansion coefficient properties make the diamond a superior MEMS material. Plasma activated wafer bonding was used in microfabrication of diamond-based CMUTs. A peak response at 5.6 MHz was measured for all ac amplitudes. Overall, diamond was demonstrated to be an applicable membrane for CMUTs.

2.2 CMUTs Theory

Generally the theory of CMUTs is based on the lumped electro mechanical approach [4]. Lumped electro-mechanical model of a CMUT element is shown in Figure 2.2. The force subjected to the mass is included spring and capacitor forces. This equation is shown in Equation 2.1.

$$F_{mass} = F_{capasitor} + F_{spring} \quad (2.1)$$

Unbiased CMUT can be considered as a simple capacitor. The stored energy in capacitor is

$$E = \frac{1}{2}CV^2 \quad (2.2)$$

The capacitor can be found by considering the potential energy stored in capacitor according to position of the mass.

$$F_{capacitor} = -\frac{d}{dx} \left(\frac{1}{2}CV^2 \right) = -\frac{1}{2}V^2 \left[\frac{d}{dx} \left(\frac{\epsilon A}{d_0-x} \right) \right] = \frac{\epsilon AV^2}{2(d_0-x)} \quad (2.3)$$

Where C is the capacitance, V is DC voltage applied to CMUT membrane and ϵ is the dielectric permittivity, A is the area of the electrodes, x is membrane displacement and d is initial separation height between electrodes.

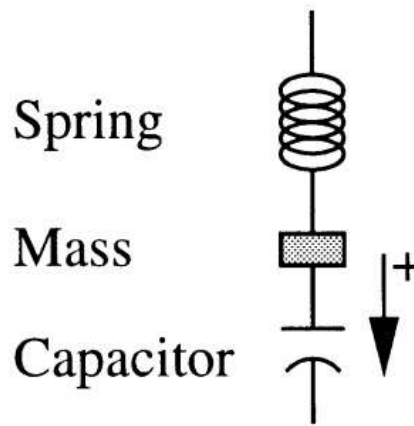


Figure 2.3 Lumped Electro Mechanical of a CMUT

The forces on the mass can be represented as the equilibrium between spring forces and electrostatic forces. Since we neglect the membrane bending and assume it to behave like a piston.

2.2.1 Collapse Voltage

Collapse voltage is one of the most important parameters for CMUT design that determines the operating point of CMUT. At this voltage value, electrostatic force becomes larger than reverse mechanical force and the membrane collapses onto the isolation layer.

Equation (2.1) can be rearranged and it gives:

$$m \frac{d^2x(t)}{dt^2} - \frac{\epsilon A[v(t)]^2}{2[d_0-x(t)]^2} + Kx(t) = 0 \quad (2.4)$$

Where k is the spring constant, and time factor can be neglected. As the voltage increases, membrane collapses because of electrostatic forces. This voltage that called collapse voltage can be considered $V(t) = V_{DC}$ and the result will be:

$$\frac{\epsilon AV_{DC}^2}{2(d_0-x)^2} = Kx \quad (2.5)$$

The resulting analytical expression gives the collapse voltage and membrane displacement values as follows;

$$V_{collapse} = \sqrt{\frac{8Kd_0^3}{27\epsilon A}} \quad (2.6)$$

$$x_{collapse} = \frac{d_0}{3} \quad (2.7)$$

As shown in equation (2.6) the collapse voltage value is proportional to the gap height and inversely proportional to the area of the capacitance plate's area. By optimizing these parameters can be obtained desired collapse voltage.

Equation (2.6) is considered the membrane is a conductor. If insulating material is used as a membrane, and dielectric permittivity between electrodes is considered, the equation will be,

$$V_{collapse} = \sqrt{\frac{8k}{27\epsilon A} \left(\frac{d_{membrane}}{\epsilon_r + d_0}\right)^3} \quad (2.8)$$

2.2.2 Snap-back Voltage

Snapback voltage is one of the characteristic parameter of the CMUT. As mention before when electrostatic force is greater than the spring force the membrane is collapsed. By decreasing the voltage the membrane does not begin to restore its shape abruptly. The voltage at which membrane leaves from substrate and goes to the original position called snap-back voltage [9]. The equation for snap-back voltage can be written as,

$$V_{snap-back} = \sqrt{\frac{2kd_{insulator}^2(d_0-d_{insulator})}{\epsilon_{insulator}A}} \quad (2.9)$$

2.2.3 Electromechanical Coupling Coefficient

Electromechanical coupling coefficient is the ratio of the produced mechanical energy to the total energy stored in the transducer [10]. The efficiency of this conversion is given in Equation (2.10).

$$k_T^2 = \frac{E_{mech}}{E_{total}} = \frac{1}{1 + \frac{E_{elec}}{E_{elec}}} \quad (2.10)$$

If the transducer is considered as a piston shape parallel plate capacitor, the equation can be written as,

$$k_T^2 = \frac{2x}{d_0 - x} \quad (2.11)$$

In equation (2.11) the membrane is considered to be conductive, if an insulator material used as membrane the equation can be rearranged,

$$k_T^2 = \frac{2x}{(d_0 + \frac{d_t}{\epsilon_r}) - x} \quad (2.12)$$

Where d_t is the membrane and insulation layer thickness and ϵ_r is the relative dielectric constant of membrane.

2.2.4 Resonance Frequency

The resonance frequency of the membrane is modelled by a mass and a spring system. In the equivalent circuit the mass is consisted of an inductor, L , where the spring is modelled by a capacitor as $1/C$ near the resonance frequency. Thus the mechanical resonance is linked to the electrical resonance as shown in following statements;

$$\omega_r = \sqrt{\frac{k}{m_e}} = \sqrt{\frac{1}{LC}} \quad (2.13)$$

Where k is the stiffness parameter and m_e is the effective mass of the membrane. Around the resonance frequency, the electrical impedance can be calculated as the equation (2.14);

$$Z_m = j(\omega L - \frac{1}{\omega C}) \quad (2.14)$$

$$\frac{\partial Z_m}{\partial \omega} = j(L + \frac{1}{C\omega^2}) \quad (2.15)$$

If the value of ω_r from equation 2.13 is inserted;

$$\frac{\partial Z_m}{\partial \omega} |_{\omega_r} = j2L \quad (2.16)$$

$$\frac{\partial Z_m}{\partial f} |_{f_r} = j4\pi m_e \quad (2.17)$$

The m_e is related to the actual mass of the membrane by using the slope of Z_m in Equation (2.17) as

$$m_e = 1.8 \rho t_m \pi a^2 \quad (2.18)$$

The resonance frequency can be written in terms of the m_e and the k as

$$f_r = \frac{2}{3\pi} \cdot \frac{t_m}{a^2} \sqrt{\frac{5Y_0}{\rho(1-\sigma^2)}} \quad (2.19)$$

2.2.5 Electrical Equivalent Circuit of CMUT

CMUTs are systems consist of electrical and mechanical parts, which are named electromechanical systems. The electromechanical system can be analyzed analytically using an equivalent electrical circuit. Voltage sources is represented mechanical forces and current sources is replaced velocities. The equivalent circuit of a CMUT is shown in Figure 2.4.

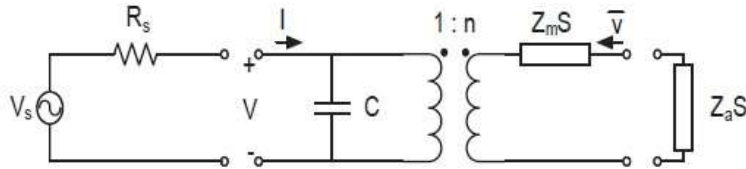


Figure 2.4 Electrical Equivalent Circuit of CMUT [9]

Transformer is represented the conversion between electrical input and mechanical output. The conversion ratio, n , shows the sensitivity of the transducer. Equation 2.21 shows that increasing membrane size or decreasing the gap between the electrodes can be improved the sensitivity of the transducer.

$$n = \frac{\epsilon_0 A}{(d_{eff} - x)^2} \quad (2.21)$$

2.3 Further CMUTs

As mentioned before, CMUTs were broadly studied and demonstrated in last decade. CMUTs with unique properties are used in medical imaging, intravascular ultrasound and airborne acoustics. For these kind of application of CMUTs, the fabrication processes are so expensive and time consuming. In order to simulate the operation of CMUTs is done with equivalent circuit model and finite element method (FEM). FEM analysis is used to predict the performance of a designed CMUT. However, FEM analysis is undesirable in design step because it has required high computational cost and many cycles to reach the steady state. Understanding the nonlinear behavior of CMUT is crucial for application which need nonlinear excitation. Nonlinear modeling of an immersed CMUT for harmonic balance was done [32]. FEM method was used for transient dynamic analysis when the membrane of CMUT is driven in nonlinear regime. Harmonic balance (HB) analysis was used in order to provide quick simulation. An equivalent circuit was designed in order to account the nonuniform velocity distribution across the membrane and predicts the nonlinear behavior of a CMUT. Better agreement between FEM and this equivalent model was observed. [32]

An improved lumped element nonlinear circuit model for circular CMUT was reported. In order to preserving the energy and power in the circuit, the force model was rederived. The model has capable to predict the entire behavior of CMUT up to the membrane touches the substrate. [33]

Parametric nonlinear lumped element model for circular CMUT in collapsed mode was reported. Collapsed membrane deflection was calculated by using the electrical force distribution in the analytical formulation of membrane deflection. Besides, lumped element model of collapsed membrane operation was developed. [34]

2.4 Application Areas of CMUTs

In total, CMUTs can be applied in two major areas: air applications, and immersion applications. In first area, the membranes should be loaded by gas or air. However, in immersion mode the membranes should be loaded by a fluid [31].

2.4.1 Air applications

In this area, temperature tolerance and better adaption to air with very high coupling efficiency, can be considered as two important advantageous. The temperature tolerance is a characteristic of the materials that used in fabrication of CMUTs. The CMUTs perfect match to air or any other gases is the best property of air application. This feature is the result of the thin membrane with low mechanical impedance.

Acoustical and electrical adapting, wider bandwidth and high electromechanical coupling efficiency are major features for air applications. NDT of fracture/crack in solids, ultrasonic ranging, and gas-flow metering are examples of air applications of CMUTs.

2.4.2 Immersion applications

In immersion CMUTs membrane is loaded with a fluid. As an illustration, the medical imaging which most of the times, is subjected by human body, can be considered as an immersion application.

There can be an immersion version for air applications ranging such as nondestructive testing (NDT) and flow metering. For example, when we do flow metering, in fluid pipes, it can be a sample of equal immersion application. High-frequency, wide-band, transducers are applied for the reduction of noise in flow-metering applications and for increasing the resolution of detection in NDT applications. Usage of one dimensional and two dimensional arrays, in immersion CMUTs for underwater and medical imaging applications, are two attractive points.

CHAPTER 3

Annular CMUT Design

Using the analytical expressions based on the CMUT theory, CMUT design parameters are calculated as shown in Table 3.1. Because these expressions are valid for circular membranes, hexagonal membranes are to be designed using the inner and outer circles contacting the hexagonal as shown in Figure 3.1. Using these results, the proper membrane thickness and side length of a hexagonal membrane are determined. Our main focus is to have a resonance frequency in the range of 500 kHz in our design.

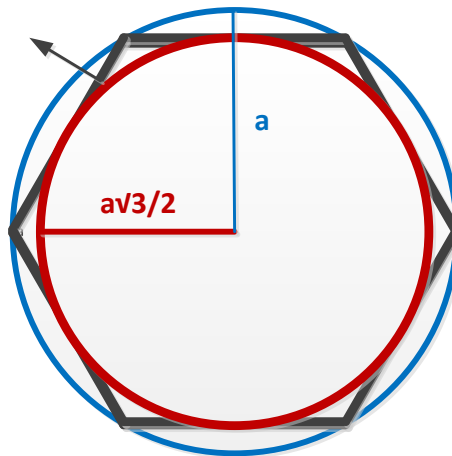


Figure 3.1 Inner and Outer Circles of a Hexagonal Membrane

Table 3.1 CMUT Design Parameters

	Membrane Thickness	$t_m = 1 \mu\text{m}$		$t_m = 3.3 \mu\text{m}$		$t_m = 5 \mu\text{m}$		$t_m = 10 \mu\text{m}$	
	Resonance Frequency (kHz)	f_{\min}	f_{\max}	f_{\min}	f_{\max}	f_{\min}	f_{\max}	f_{\min}	f_{\max}
Membrane Radius	50 μm	101	135	334	446	507	676	1014	1353
	60 μm	70	94	232	310	352	470	704	939
	70 μm	51	69	170	277	258	345	517	690
	80 μm	39	52	130	174	198	264	396	528

3.1 Disk CMUT Mask Designing

Developing a transducer, several photolithographic steps are included. One particular mask for each etching or deposition step is required. The photolithography technique was used for patterning layers of the CMUT. The layout for a set of three masks was created using Tanner EDA L-Edit software, where each layer in the design represents a mask. All fabrication processes are went along by process rules. The masks are square glass plates and have size 5" corresponding to the 4" wafer size as the most compatible as shown in figure 3.2.

Fine alignment marks are placed in two rectangular areas on the left and right sides of the wafer surrounded by a frame box as shown in Figure 3.3. They allow alignment accuracy up to 1 μm using the lower aligning crosses. Below the alignment marks \Photolitho" pattern can be found for checking the exposure resolution.

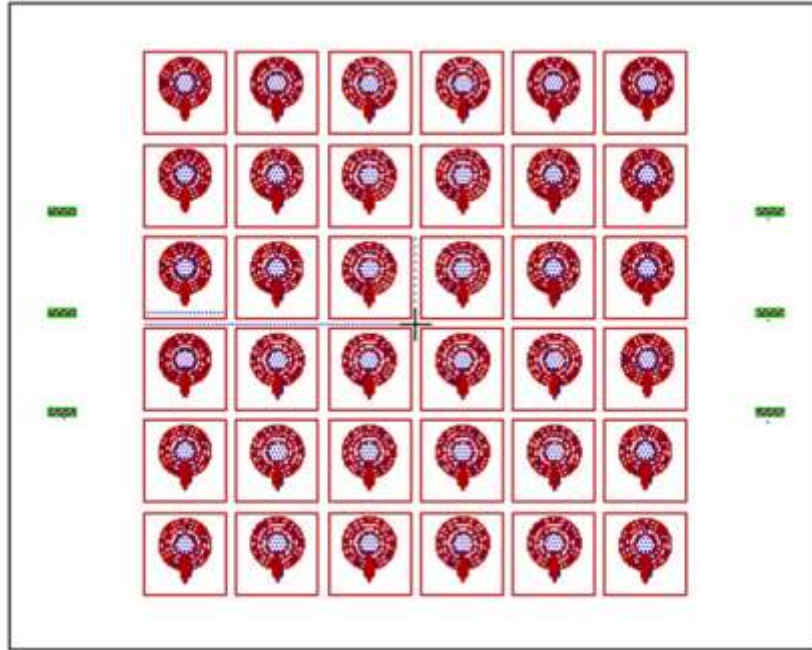


Figure 3.2 Mask Plate

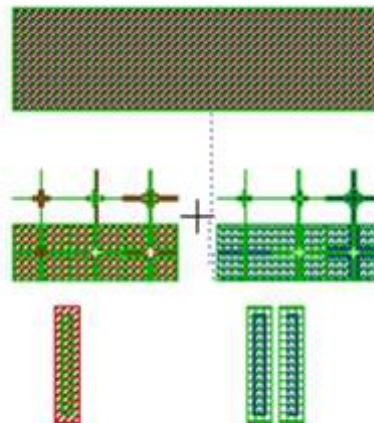


Figure 3.3 Alignment

A Disk CMUT with a circular shape which includes several cells is chosen. The circle is divided to four parts. These parts are filled with cells in hexagon shape. The number of hexagons in each part is same to have a same capacitance value, a disk CMUT is shown in figure 3.4. Several designs of CMUT cells have been made to evaluate the most suitable one.

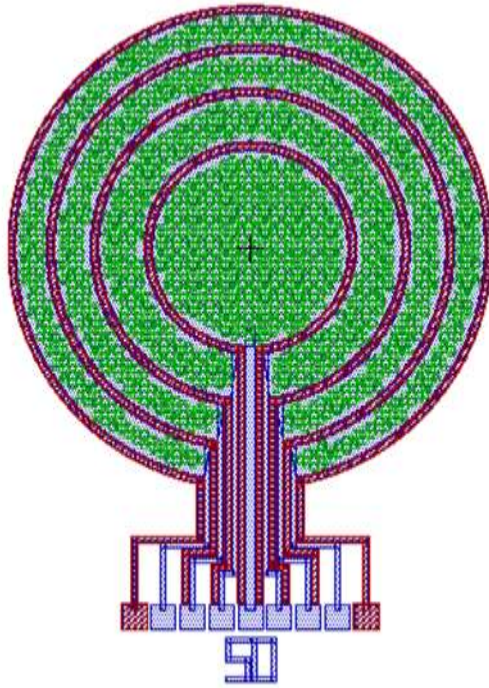


Figure 3.4 CMUT disk mask with hexagon cells

In the piezoelectric transducer the whole surface of the transducer is moving and therewith providing an efficient emitting and receiving surface area. In a CMUT device the transmitting and emitting surface area includes of many individual cells. The cells have to be supported and the support structures create a “dead” area on the surface. In transmitting mode the dead area is decreasing the power of the ultrasound wave. It is important to reduce the inactive area of the CMUT. Two main considerations can be produce to prevent this problem. The cells have to be as close as possible to each other. The limit is how thin the support walls can be created. It can both be a process restriction and an adherence problem to get adequate adherence of the membrane to the substrate. Second, the design of the individual cells impress how well they fit to each other. Several published designs [13, 14] are based on a hexagonal structure of the cell. This pattern gives a high packing density. The hexagonal cell is however more difficult to model and the behavior must be examined in numerical analysis. A circular membrane is easier modeled and can give fairly consistent results from both analytical and numerical analysis. This work uses a hexagonal cell in order to reach the better fill factor.

The cell sizes are decided to increase the success of manufacturing process and have different resonance frequencies. While the cell size increases, the resonance frequency decreases and gap height needs to be increased due to air collapse. In order to reach this goal, we designed 4 masks with different cell size, 50 μm , 60 μm , 70 μm and 80 μm . The lithography step includes three masks: 1. CAVITY 2. TOPLAYER 3.CAVITY

CAVITY mask create the hexagon cells on the wafer; TOPLAYER mask is defined the etching process and the 3rt mask is belong to metallization.

3.2 Disk CMUT Mask with 50 μm hexagon cells

As is mentioned before, disk CMUT has a circular shape that divided to four parts, one circle in the middle and 3 disks in behinds. The total inner radius of circle is 2.5 mm. A 20 μm thin ground disk is created between every part. The surface of all parts is composed of many hexagons cells. In first mask the cell size is chosen 50 μm .

3.2.1 Steps of drawing 1st mask: CAVITY

In order to create cavity mask a code based algorithm is developed thanks to custom macro support of L-Edit. C programming language is used as the basis of this macro. For each cell size, a custom function is created. This function improved the design accuracy and allowed to obtain error-free design. It is possible to create a CMUT layout with any cell size and cell-to-cell separation in a minute by changing required parameters. When we load this macro one window that shown in figure 3.5 is opened, and from this window the properties of the mask can be inputted.

In the next step, a new layer in layer palette is created with 1CAVITY name and the green is chosen as its color.

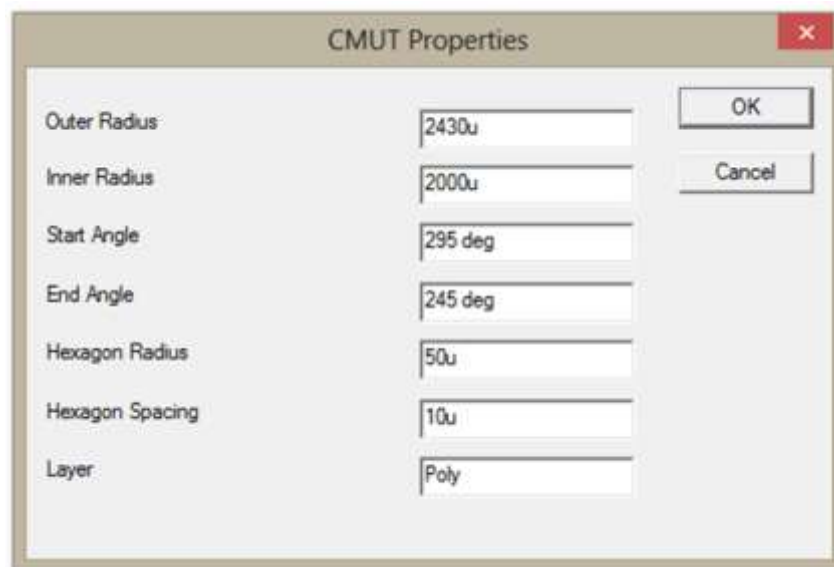


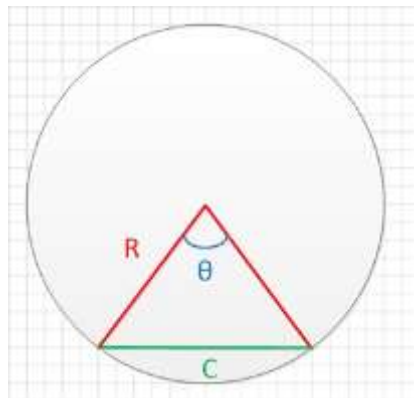
Figure 3.5 the property window of Macro

Table 3.2 shows the properties of the 1st mask that we used as inputs for macro to create the cavity.

Table 3.2 Macro inputs for CAVITY mask with 50 μm hexagonal cells.

AREA	A ₁	A ₂	A ₃	A ₄
Outer Radius	1013	1567	2025	2430
Inner Radius	0	1103	1657	2115
Start Angle	270.001	277.24	279.67	281.42
End Angle	270	262.76	260.33	258.58
Hexagon Radius	50	50	50	50
Hexagon Spacing	10	10	10	10
Number of cells	360	359	360	360

The A₁ is in circle shape, so inner radius of it is 0; the angle is 0, too, but the A₂, A₃, A₄ are in disk shape but because of the electrodes that attached them, they are not complete disk, so an angle for these parts is defined that this angle is calculated with equation 1.



$$\theta = 2 \arcsin (C/2R) \quad (3.1)$$

The figure 3.6 shows the cavity mask for 50μm hexagon cells, and the figure 3.7 is the microscope picture of this mask.

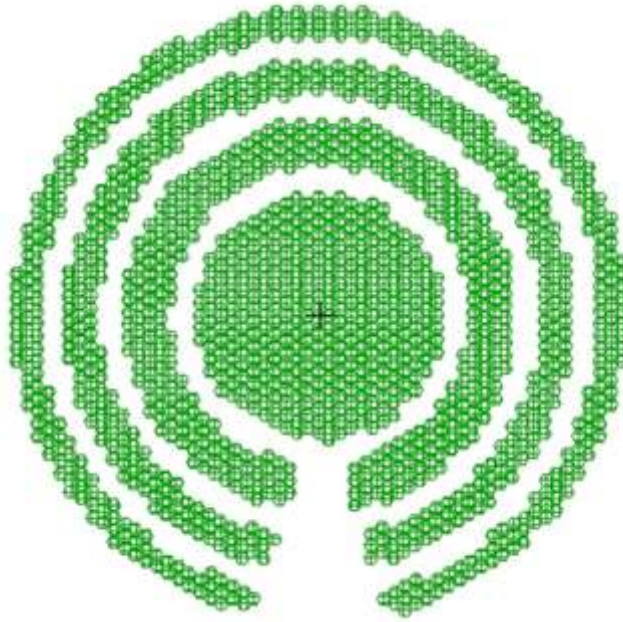


Figure 3.6 CAVITY mask with 50 μ m hexagon cells

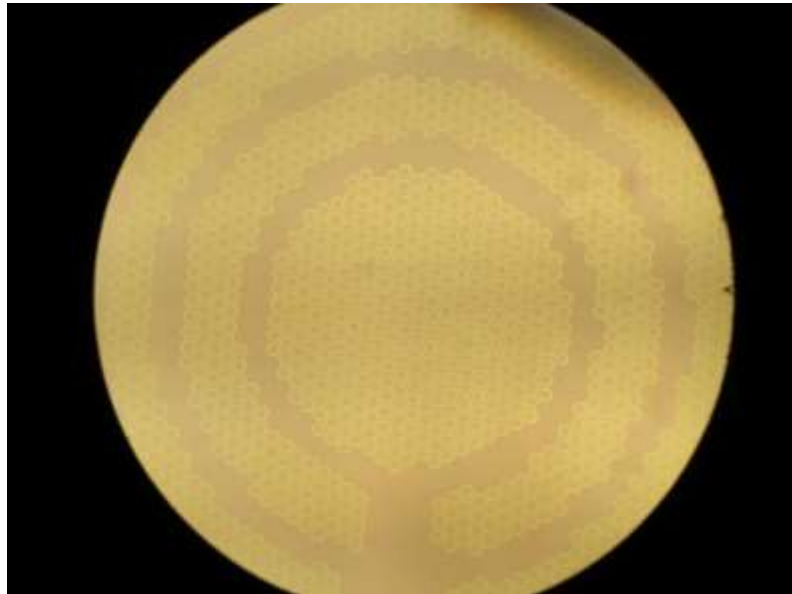


Figure 3.7 CAVITY mask with 50 μ m hexagons (central view, x5 lens)

3.2.2 Steps of drawing 2nd mask: TOPLAYER

As was mentioned before 2nd mask is etching mask, in order to develop this, a new layer is created with 2TOPLAYER (Gds: 20) name and red as its color is chosen. For drawing this mask a kind of shape that its name is Tori that exist in Tanner library was used, this shape have properties like inner radius, outer radius, start angle and end angle, that with adjusting them, desire shapes can be drawn. The Tori is shown in figure 3.8.

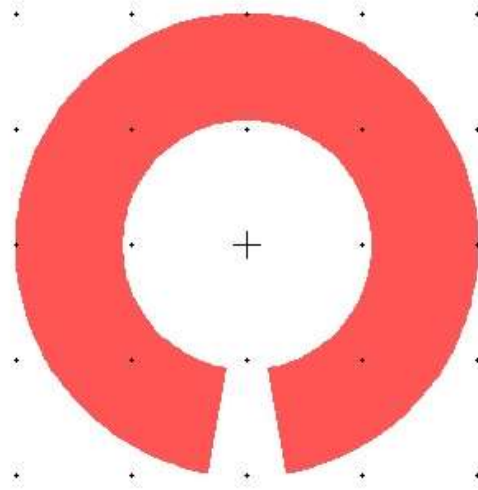


Figure 3.8 Tori

This mask is containing 4 parts that is separated to A₁, A₂, A₃ and A₄ areas. The thickness of these parts is 70 μm . In metallization step between these areas, GND layers will be created, and this mask needs electrodes to connect areas to pads. Figure 3.9 shows the 2nd mask.

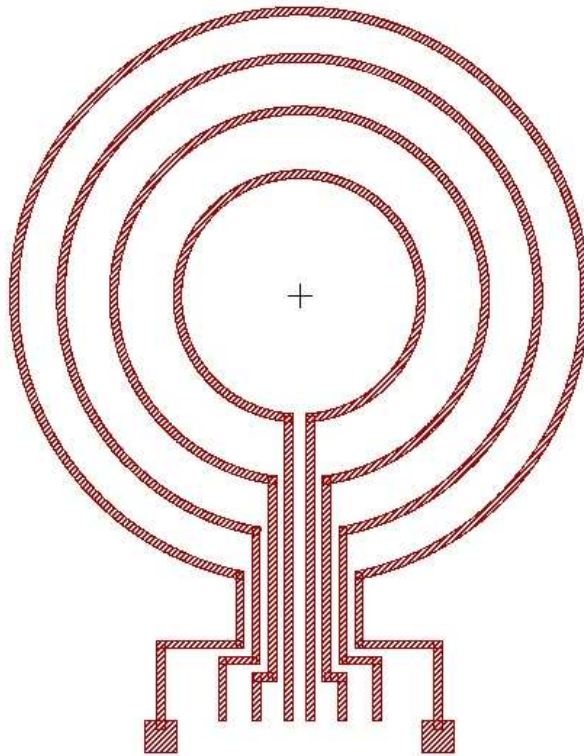


Figure 3.9 TOPLAYER Mask for 50 μm hexagonal cells

The main property of this mask is its symmetric shape, so this kind of design has double padding. The pads with $250\ \mu\text{m} \times 250\ \mu\text{m}$ dimensions are belonged to GND. Table 3.3 shows the physical dimensions of 2nd mask.

Table 3.3 TOPLAYER Mask Properties with 50 μm hexagonal cells

Area	GND1	GND2	GND3	GND4
Outer radius	1093	1647	2105	2510
Inner radius	1023	1577	2035	2440
Start angle	273.362	277.28	279.617	281.345
End angle	266.638	262.72	260.383	258.655

3.2.3 Steps of drawing 3rd mask: METAL

In order to have electrically connection between cells, metallization is needed; so the 3rd and last mask is metallization mask. This mask covered the hexagon cells, GND layers, electrodes and pads. For covering the hexagons the same values that use in macro was used. Between every area there is 50 μm GND layer, and the thickness of the electrodes is 50 μm , too. For drawing this mask, at first a new layer with 3METAL name (Gds: 30) was created, and blue as its color was chosen. The table 3.4 shows the physical dimensions of the 3rd mask.

Table 3.4 METAL Mask Properties with 50 μm hexagonal cells

Area	A1	GND1	A2	GND2	A3	GND3	A4	GND4
Outer radius	1013	1083	1567	1637	2025	2095	2430	2500
Inner radius	0	1053	1103	1587	1657	2045	2115	2450
Start angle	270.00 1	273.841	277.24	277.603	279.67	279.854	281.42	281.536
End angle	270	266.159	262.76	262.397	260.33	260.146	258.58	258.463

The figure 3.10 shows the 3rd (METAL) mask.

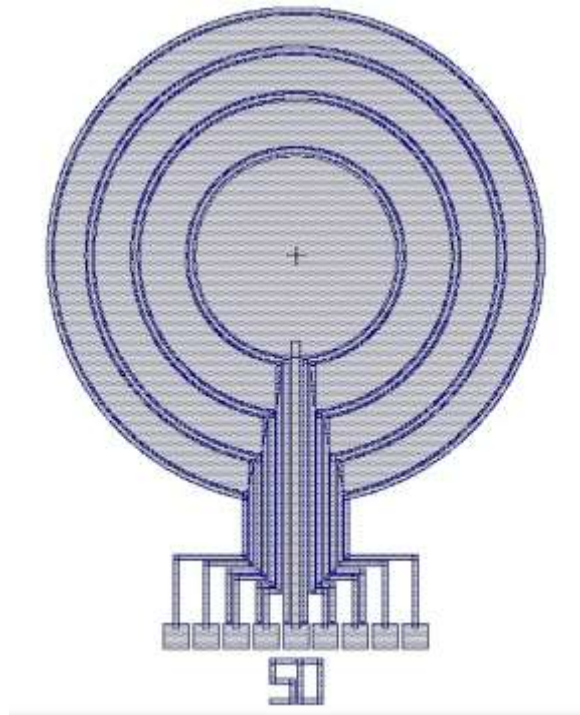


Figure 3.10 METAL Mask for 50 μm hexagonal cells

3.3 Disk CMUT mask with 60 μm hexagon cells

In this mask the size of the hexagon cells are 60 μm , but the other parts of the design is same.

3.3.1 Steps of drawing 1st mask: CAVITY

The figure 3.11 shows the cavity mask for 60 μm hexagon cells.

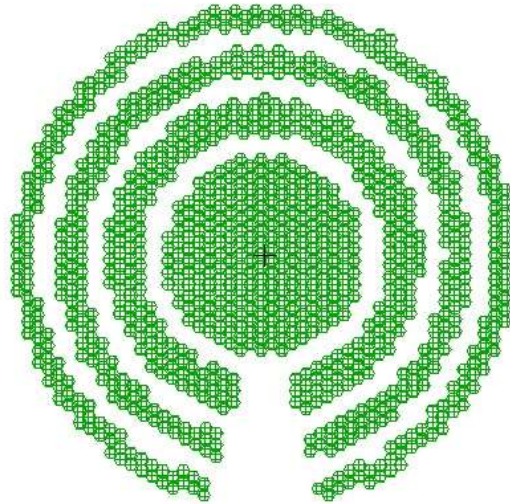


Figure 3.11 CAVITY mask with 60 μ m hexagon cells

Table 3.5 shows the properties of the 1st mask that was used as inputs for macro to create the cavity.

Table 3.5 Inputs of Macro for CAVITY mask with 60 μ m hexagonal cells

Area	A1	A2	A3	A4
Outer radius	1013	1570	2030	2445
Inner Radius	0	1103	1660	2120
Start angle	270.001	277.24	279.71	281.42
End angle	270	262.76	260.29	258.58
Cell size (μ m)	60	60	60	60
Hexagon Spacing (μ m)	10	10	10	10
Number of cells	254	253	254	254

3.3.2 Steps of drawing 2nd mask: TOPLAYER

Figure 3.12 shows the 2nd mask.

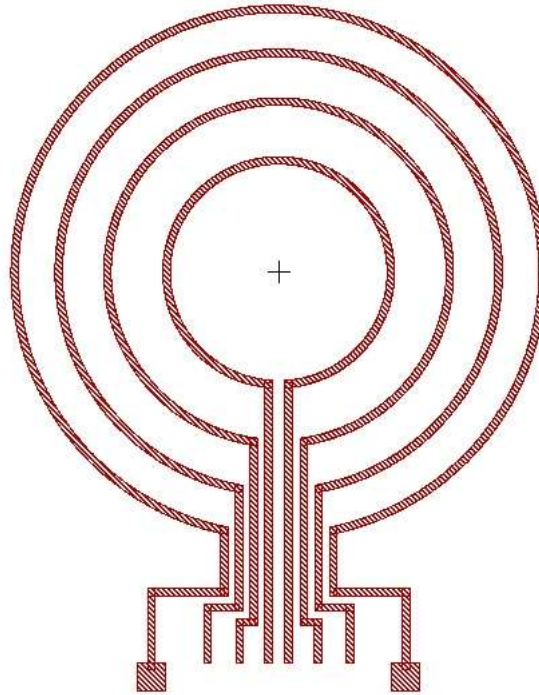


Figure 3.12 TOPLAYER Mask for 60µm hexagon cells

Table 3.6 shows the physical dimensions of 2nd mask.

Table 3.6 TOPLAYER Mask Properties with 60 µm hexagonal cells

Area	GND1	GND2	GND3	GND4
Outer Radius	1093	1650	2110	2525
Inner Radius	1023	1580	2040	2455
Start angle	273.62	277.272	279.59	281.27
End angle	266.38	262.728	260.41	258.73

3.3.3. Steps of drawing 3rd mask: METAL

Table 3.7 shows the physical dimensions of the 3rd mask.

Table 3.7 METAL Mask Properties with 60 μm hexagonal cells

Area	A1	GND1	A2	GND2	A3	GND3	A4	GND4
Outer radius	1013	1083	1570	1640	2030	2100	2445	2515
Inner radius	0	1033	1103	1590	1660	2050	2120	2465
Start angle	270.001	273.841	277.24	277.58	279.71	279.83	281.42	281.46
End Angle	270	266.159	262.76	262.42	260.29	280.17	258.58	258.54

Figure 3.13 shows the 3rd (METAL) mask.

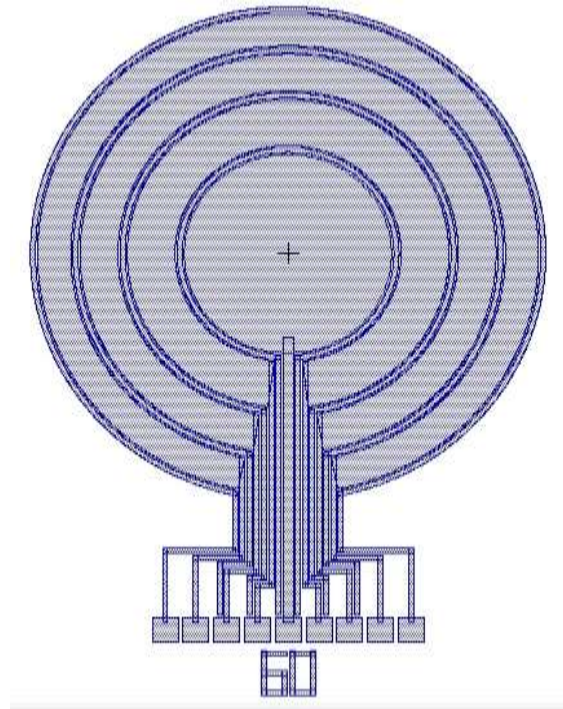


Figure 3.13 METAL Mask for 60 μ m hexagon cells

The figure 14 shows the total masks of Disk CMUT with 60 μ m hexagon cells.

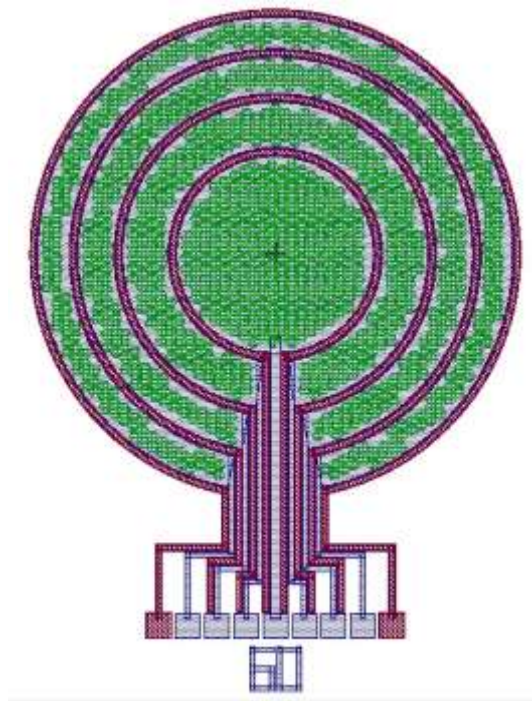


Figure 3.14 CMUT disk mask with 60 μ m hexagon cells

3.4 Disk CMUT mask with 70 μm hexagon cells

In this mask the size of the hexagon cells are 70 μm , but the other parts of the design is same.

3.4.1 Steps of drawing 1st mask: CAVITY

The figure 15 shows the cavity mask for 70 μm hexagon cells.

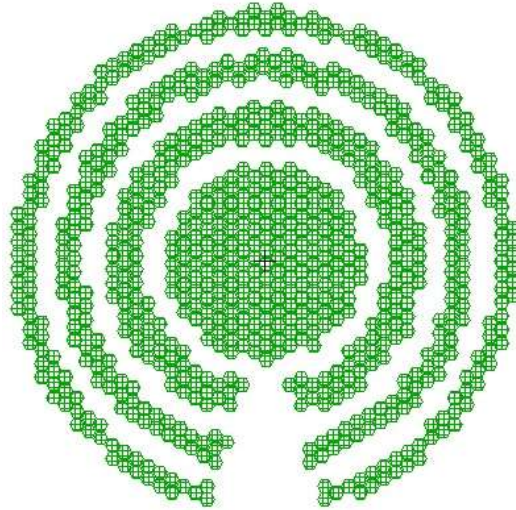


Figure 3.15 CAVITY mask with 70 μm hexagon cells

Table 3.8 shows the properties of the 1st mask that we used as inputs for macro to create the cavity.

Table 3.8 Inputs of Macro for CAVITY MASK with 70 μm hexagonal cells

Area	A1	A2	A3	A4
Outer radius	1013	1587	2072	2495
Inner radius	0	1103	1677	2162
Start angle	270.001	277.24	279.611	281.2
End angle	270	262.76	260.389	258.8
Cell size (μm)	70	70	70	70
Cell spacing	10	10	10	10

3.4.2 Steps of drawing 2nd mask: TOPLAYER

Figure 16 shows the 2nd mask.

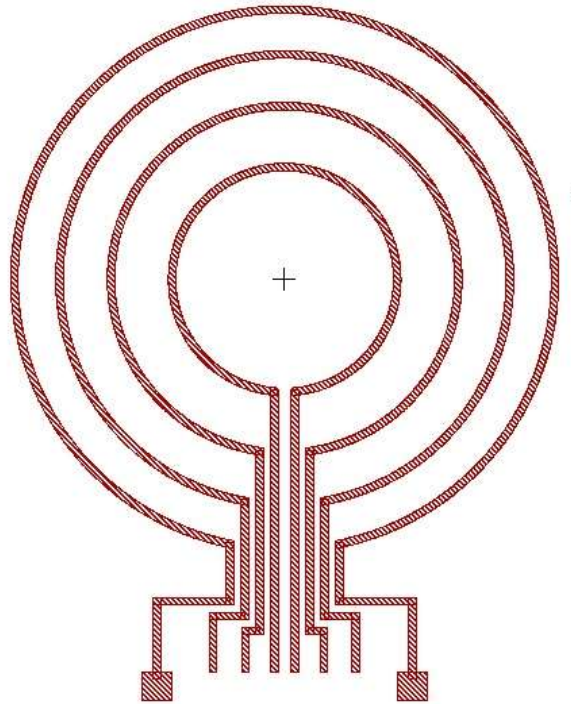


Figure 3.16 TOPLAYER Mask for 70µm hexagon cells

Table 3.9 shows the physical dimensions of 2nd mask.

Table 3.9 TOPLAYER Mask Properties for 70µm hexagon cells

Area	GND1	GND2	GND3	GND4
Outer radius	1093	1667	2152	2575
Inner radius	1023	1597	2082	2505
Start angle	273.62	277.19	279.398	281.04
End angle	266.38	262.81	260.612	258.96

3.4.3 Steps of drawing 3rd mask: METAL

Table 3.10 shows the physical dimensions of the 3rd mask.

Table 3.10 METAL Mask Properties for 70 μ m hexagon cells

Area	A1	GND1	A2	GND2	A3	GND3	A4	GND4
Outer radius	1013	1093	1587	1667	2072	2152	2495	2575
Inner radius	0	1023	1103	1597	1677	2082	2162	2505
Start Angle	270.01	273.62	277.24	277.19	279.61	279.39	281.04	281.04
End Angle	270	266.38	262.76	262.81	260.38	260.61	258.96	258.96

Figure 3.17 shows the 3rd (METAL) mask.

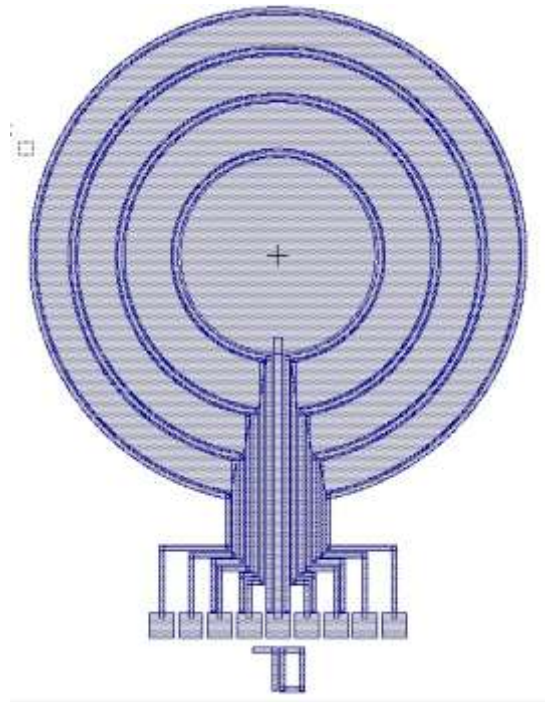


Figure 3.17 METAL Mask for 70 μ m hexagon cells

The figure 3.18 shows the total masks of Disk CMUT with 70 μ m hexagon cells.

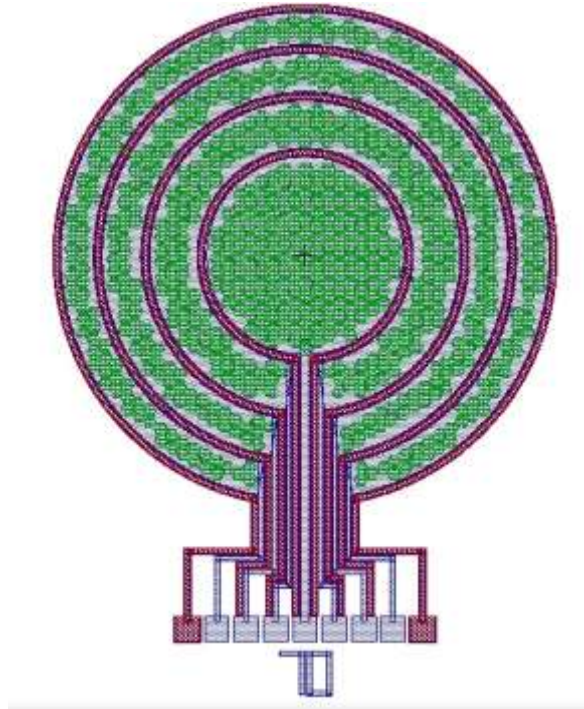


Figure 3.18 CMUT disk mask with 70 μm hexagon cells

3.5 Disk CMUT mask with 80 μm hexagon cell

In this mask the size of the hexagon cells are 80 μm , but the other parts of the design is same.

3.5.1 Steps of drawing 1st mask: CAVITY

Figure 3.19 shows the cavity mask for 80 μm hexagon cells.

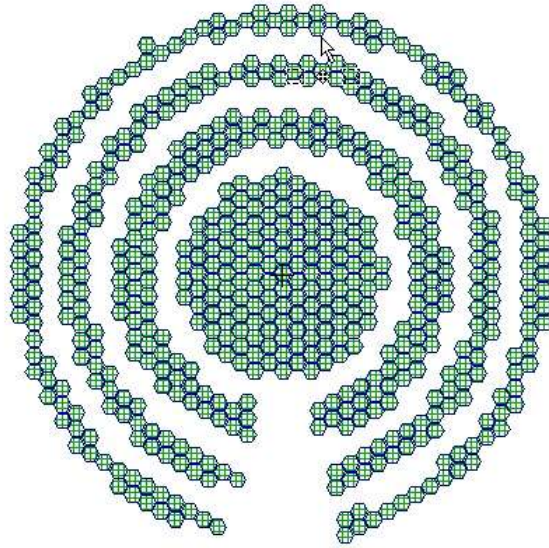


Figure 3.19 CAVITY mas with 80 μ m hexagon cells

Table 3.11 shows the properties of the 1st mask that we used as inputs for macro to create the cavity.

Table 3.11 Inputs of Macro for CAVITY mask with 80 μ m hexagonal cells

Area	A1	A2	A3	A4
Outer radius	1013	1595	2076	2508
Inner radius	0	1103	1685	2166
Start angle	270.001	277.24	279.565	281.18
End angle	270	262.76	260.435	258.82
Cell size (μ m)	80	80	80	80
Cell spacing (μ m)	10	10	10	10
Number of cells	143	142	143	143

3.5.3 Steps of drawing 3rd mask: METAL

Table 3.13 shows the physical dimensions of the 3rd mask.

Table 3.13 Metal Mask Properties for 80 μ m hexagon cells

Area	A1	GND1	A2	GND2	A3	GND3	A4	GND4
Outer radius	1013	1083	1595	1665	2076	2146	2508	2578
Inner radius	0	1033	1103	1615	1685	2096	2166	2528
Start angle	270.01	273.84	277.24	277.47	279.56	279.61	281.18	281.17
End Angle	270	266.15	262.76	262.53	260.43	260.39	258.82	258.73

The figure 3.21 shows the 3rd (METAL) mask.

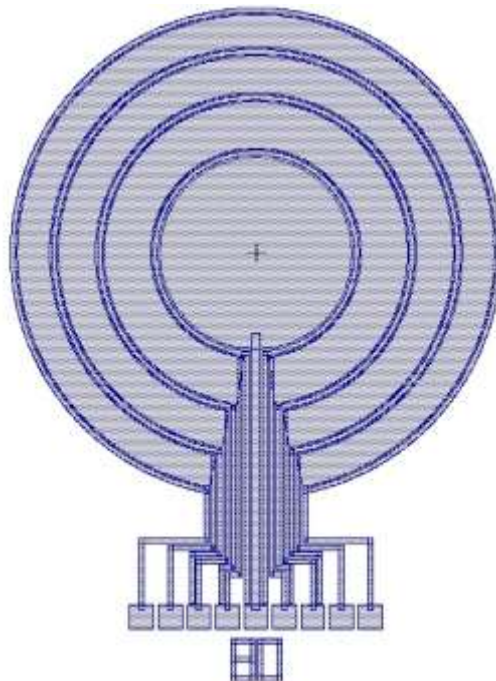


Figure 3.21 METAL Mask for 80 μ m hexagon cells

Figure 3.22 shows the total masks of Disk CMUT with 80 μ m hexagon cells.

Designed layout mask for CMUT cells is transferred to a quartz mask in order to be used in photolithographic process.

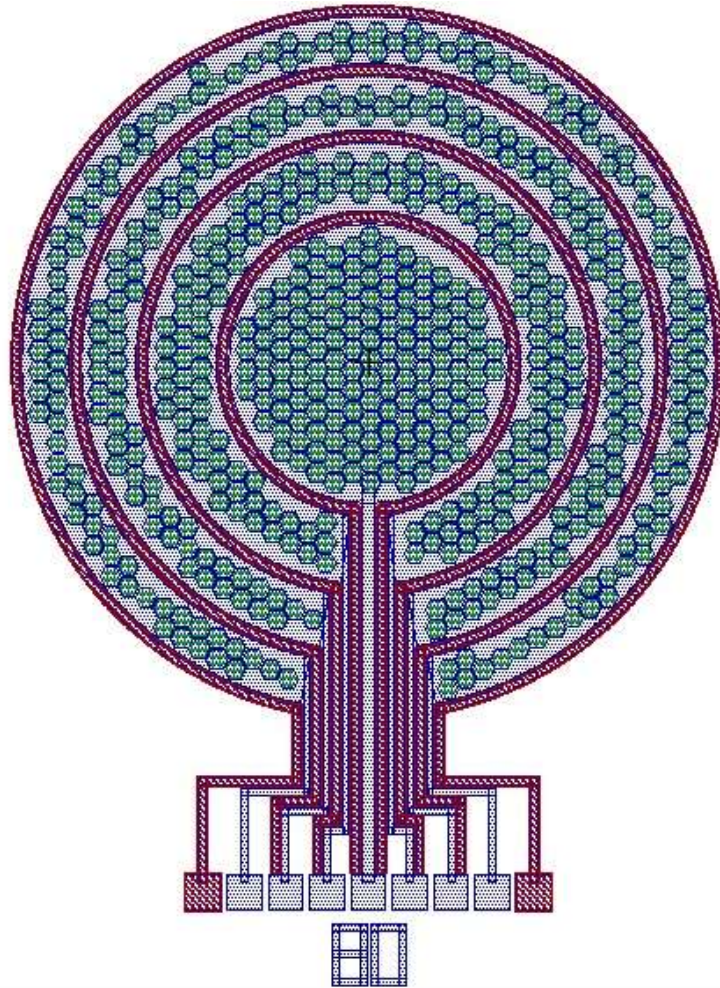


Figure 3.22 CMUT disk mask with 80 μ m hexagon cells

CHAPTER 4

DIAMOND MEMBRANE CHARACTERIZATION FOR CMUT's

Residual stress of a membrane material in capacitive micromachined ultrasonic transducer (CMUT) is a critical parameter that affects the CMUT operation. A nondestructive technique that obtained noticeable popularity in the field of residual stress measurements is Raman spectroscopy. A new age of diamond films which used as a membranes in CMUTs are UNCD and NCD films. Hot Filament Chemical Vapor Deposition (HFCVD) system is used for the deposition of rigid and smooth Nanocrystalline Diamond (NCD) and Ultra Nanocrystalline Diamond (UNCD) thin films on 4 inch silicon substrate.

4.1 Diamond as a Membrane Material

Diamond is an encouraging MEMS substance due to its high Young's Modulus and very large thermal conductivity. Diamond is a reliable and robust material which makes it proper to be used as a membrane of the CMUTs. The most important disincensive of the diamond film utilization is associated with the poor adhesion strength of CVD diamond films to a variety of substrates (Si, WC1Co, metal, etc.). This is due to the high residual stress inherent in the film as a result of the CVD processing. Therefore, understanding the origins of the diamond film stresses, their exact measurement and subsequent relaxation techniques play the key role in the application of the diamond films in the modern technology.

4.2 Stress Measurements Techniques

Residual stresses in thin films are typically measured by the curvature mode, XRD and Raman spectroscopy methods. The curvature method uses parallel incident laser beams which provides the possibility for the measurement of the wafer's curvature and the residual stress. In this process, observation of the location of the reflected beams gives the wafer's curvature and the residual stress in a straightforward manner with the aid of the Stoney's equation. Another alternative is to use peak shift procedure which is indirect and applicable in a case that the film curvature is not traceable. When the crystal is elastically distorted under stress, the positions of the diffracted X-ray beam or Raman peak are shifted as crystal are elastically distorted under stress. However, the experimental data obtained by these methods, have a substantial amount of disparity on the magnitude of residual stresses in the diamond films. The measured stress values are widely diverse and differ in the sign even for the same diamond/Si specimen from a CVD system.

In this chapter, Raman spectroscopy will be explained as a stress measurement method. The curvature technique is typically applicable before the deposition process. Therefore, this method is not beneficial for the stress measurement of our wafers. The other alternative is XRD method which is applicable on single crystalline materials because their grain sizes are the same. However, the wafers used in our process were polycrystalline and the grain sizes are not the same. Therefore, the mentioned XRD technique is not practicable on our polycrystalline or amorphous films. Table 4.1 shows the difference between these methods.

Table 4.1 Stress Measurement Techniques

Techniques	Method Requirements	Material Requirements
Curvature Method	Before/After Deposition	All Materials
XRD	–	Single Crystalline
Raman	–	Single/Polycrystalline

4.3 Raman spectroscopy

Raman spectroscopy is one of the popular ways used widely to identify diamond, graphite and other carbon-base materials. The first-order Raman spectrum of diamond has a single line at 1332cm^{-1} . The spectrum with a single high-frequency line at about 1580cm^{-1} is belonged to large single-crystal graphite. Raman spectrum for amorphous carbon consists of two broad peaks around $1200\text{--}1450\text{cm}^{-1}$ for the D band and $1500\text{--}1700\text{cm}^{-1}$ for the G band. The G band is ascribed to graphite-like layers of sp^2 micro-domains, while the D band is attributed to the bond-angle disorder in the sp^2 graphite-like micro-domains induced by the linking with sp^3 carbon atoms as well as the finite crystalline sizes of sp^2 micro-domains. In Raman spectroscopy, position of the diamond peak shifts to higher (lower) frequency under the compressive (tensile) stress, and the shift amount is related to the stress in the diamond film.

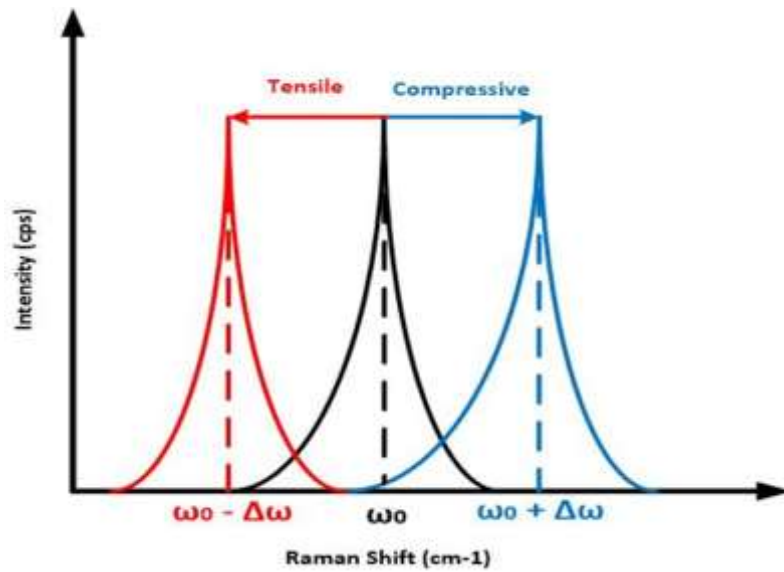


Figure 4.1 Diagram of Raman peak

$$\sigma_f = M_f \Delta\omega / \omega_0 \gamma \quad (4.1)$$

$$\sigma_f = -1.08 \Delta\omega \quad (4.2)$$

Where ω_0 and $\Delta\omega$ are the position of the diamond peak under the stress-free condition and the subsequent peak shift respectively, M_f are the biaxial Young's moduli of diamond film that is 850 GPa for UNCD films and 1000 GPa for NCD films, and γ the Gruneisen parameter of diamond (0.94~ 1.19) .

4.4 Raman Measurement Results

The wafers which are utilized as a CMUT membrane, are MCD, NCD and UNCD. The difference between these wafers is their grain sizes as shown in table 4.2. The stress exists in different films directly affects their adhesion quality and causes them to delaminate from the substrate. In the present chapter, the amount of compressive and tensile stress is shown in MCD, NCD and UNCD films. The films were characterized by different grain sizes, different doping states and different thicknesses to provide the best membrane material for CMUT's.

Table 4.2 Properties of MCD, NCD and UNCD

Type of Diamond Film	Grain Size	Young's Modulus
MCD	Several Micrometers	~ 1000 GPa
NCD	10 to 100 Nanometers	1000 GPa
UNCD	Less than 10 Nanometers	850 GPa

4.4.1 UNDOPED MCD

The Raman shift of UNDOPED MCD is shown in Figure 4.2. The thickness of the diamond which is deposited on top of the silicon is 0.8 μm as shown in table 4.3. The measured plot consists of two sharp peaks. One of them which is located in 520 cm^{-1} is belonged to Si, and the other peak belongs to the diamond near the 1320 cm^{-1} . Since, the diamond peak shifts a little to a higher frequency, the UNDOPED MCD wafer has a tensile stress. This point determines the desirable material that can be used as a membrane of the CMUT. In order to calculate the stress value, the shift value should be substituted in equation 1. As shown in table 4.3, the stress value for UNDOPED MCD is very low, and this property makes it very desirable for CMUT membrane usage.

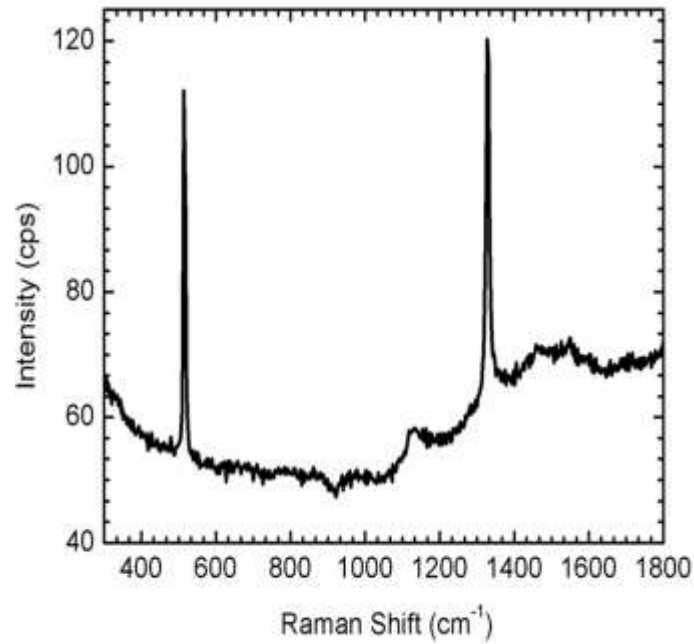


Figure 4.2 Spectrum of UNDOPED MCD

Table 4.3 UNDOPED MCD PROPERTIES

Diamond Thickness (μm)	Doping State	Base Wafer	Stress Value (MPa)
0.8	UNDOPED	Si	+125 (tensile)

4.4.2 DOPED MCD

The special property which makes the utilization of Boron-Doped wafers popular in the field of CMUT's is their conductivity. In the mentioned wafer, the thickness of the diamond is 0.8 μm like UNDOPED MCD. But, there are no sharp peaks because of the doping state as shown in figure 4.2. The stress value is near zero and tensile as shown in table 4.4.

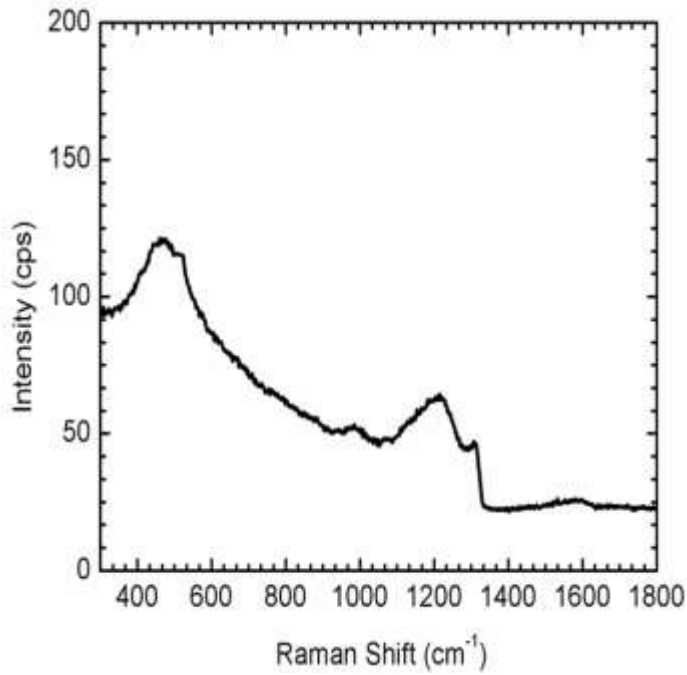


Figure 4.3 Spectrum of DOPED MCD

Table 4.4 DOPED MCD PROPERTIES

Diamond Thickness (μm)	Doping State	Base Wafer	Stress (MPa)	Value
0.8	Boron-Doped	Si	+233 (tensile)	

4.4.3 UNDOPED NCD

In NCD wafers, there are three broad peaks unlike MCD wafers as shown in figure 4.4. This is because of the fact that, small grain size and large grain boundary can't be seen as sharp peaks. In the plot, one peak belongs to Si in 520 cm^{-1} and the peak around 1320 cm^{-1} stands for the D band and 1550 cm^{-1} related to the G band. The properties of the UNDOPED NCD is shown in the table 4.5. The measured stress value is found to be compressive which is not desirable. Si peak is small because of the base wafer as shown in figure 4.4. There is also a thin layer of SiO_2 between the Si substrate and diamond

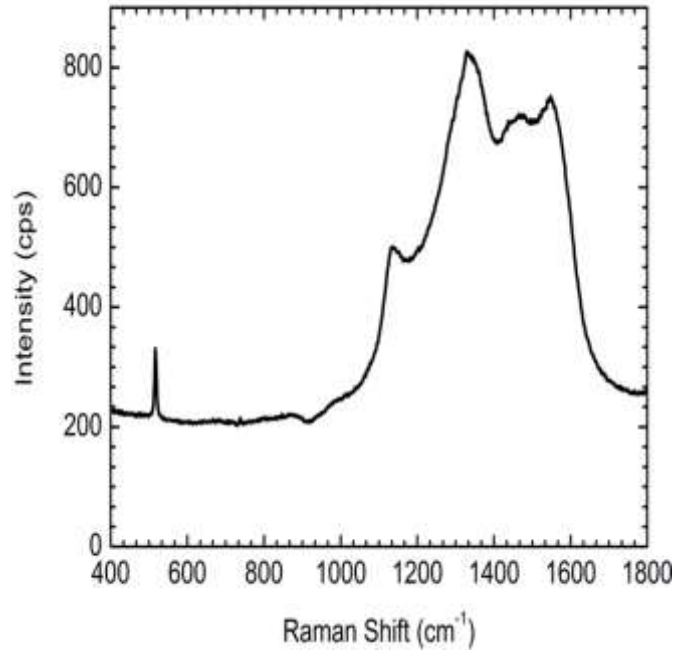


Figure 4.4 Spectrum of UNDOPED NCD

Table 4.5 Properties of UNDOPED NCD

Diamond Thickness (μm)	Doping State	Base Wafer	Stress Value (MPa)
1.7	UNDOPED	Si/SiO ₂	-12.6 (Compressive)

4.4.4 DOPED NCD

In DOPED NCD, the thickness of the diamond is about 3.5 μm as shown in table 4.6. The mentioned thickness is higher than the UNDOPED one. Therefore, the diamond peak is located at the stronger point with respect to the Si peak as shown in figure 4.5. Here, the stress value is tensile.

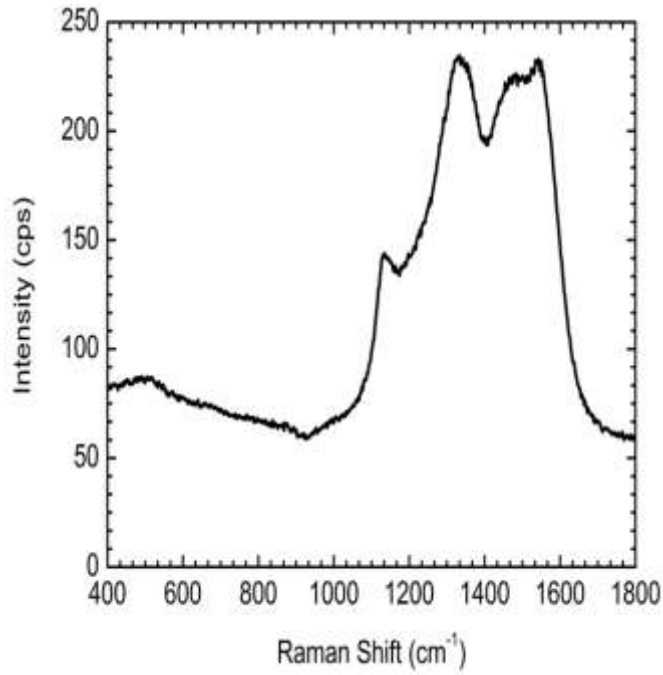


Figure 4.5 Spectrum of DOPED NCD

Table 4.6 Properties of DOPED NCD

Diamond Thickness (μm)	Doping State	Base Wafer	Stress Value(MPa)
3.5	Boron-Doped	Si	+153 (tensile)

4.4.5 UNDOPED UNCD

As mentioned before, the grain size of the UNCD wafer is less than 10 nm. Therefore, the peaks in the D-band and G-band of Raman spectrum is broad. In order to find the maximum position for each peak, the Lorentz fit was used. Since, the stress values found for the mentioned wafers is relatively high as shown in table 4.7, they are not desirable for the membrane usage.

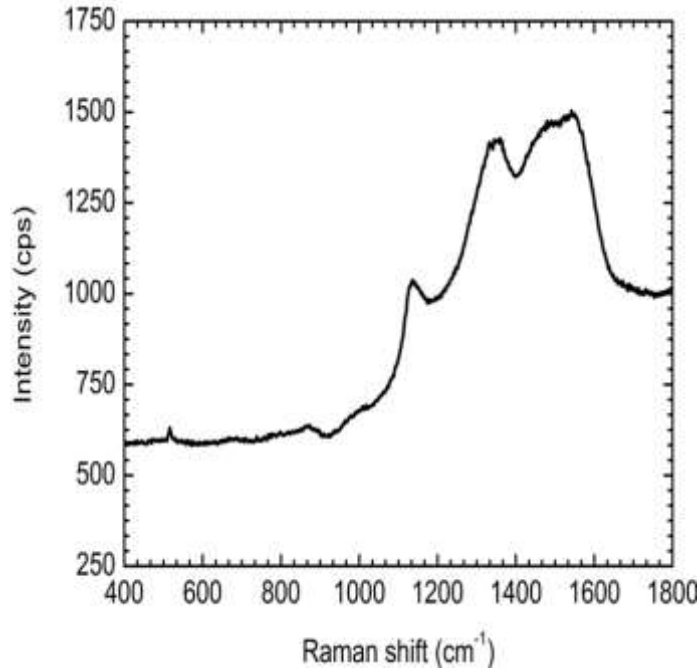


Figure 4.6 Spectrum of UNDOPED UNCD

Another kind of UNCD was analyzed with thinner deposited diamond as shown in figure 4.7. Because, in this case the stress value is lower in comparison to the thicker UNCD. However, the nature of the stress is the same as shown in table 4.7.

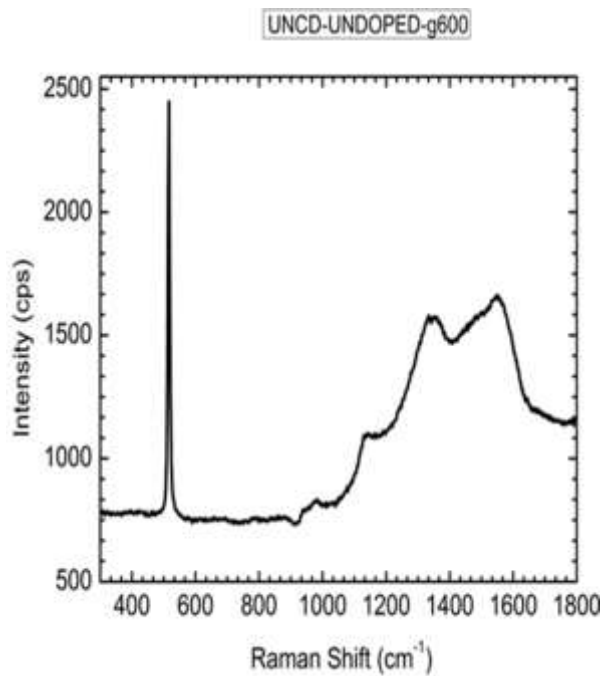


Figure 4.7 Spectrum of UNDOPED UNCD with 0.3 μm thickness

The stress value in compare with thicker UNCD is a little low, but the nature of the stress is same. The properties of this wafer are shown in table 4.7.

Table 4.7 Properties of UNDOPED UNCD

Diamond Thickness (μm)	Doping State	Base Wafer	Stress Value (MPa)
1.0	UNDOPED	Si	-385 (compressive)
0.3	UNDOPED	Si	-178 (compressive)

4.4.6 DOPED UNCD

The thickness of the DOPED UNCD is as same as the UNDOPED one. The nature of the stress is tensile but the value is high as shown in table 4.8.

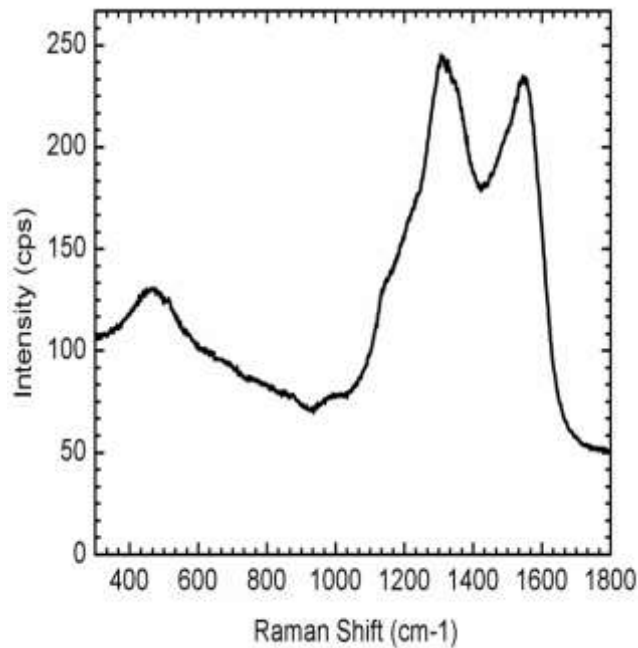


Figure 4.8 Spectrum of DOPED NCD

In the thinner DOPED UNCD, the stress nature is the same but in a lower value with respect to the thicker one as shown in table 4.8.

Table 4.8 Properties of DOPED UNCD

Diamond Thickness (μm)	Doping State	Base Wafer	Stress Value (MPa)
1.0	Boron-Doped	Si	+364 (tensile)
0.3	Boron-Doped	Si/SiO ₂	+244 (tensile)

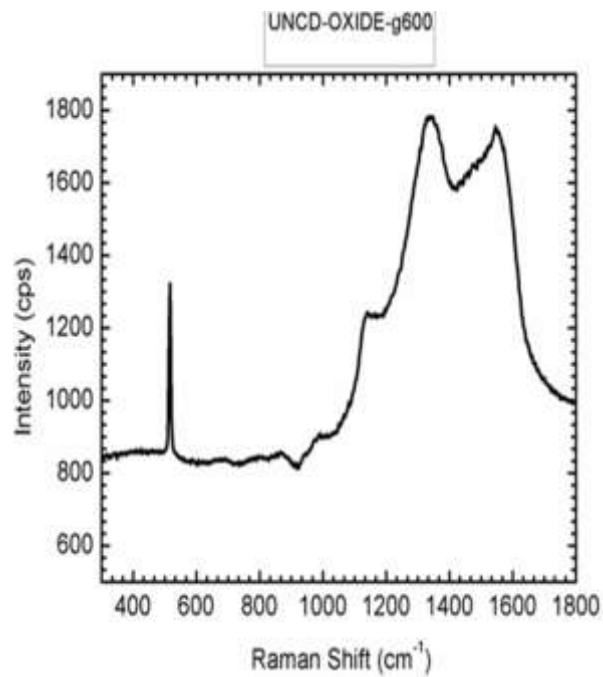


Figure 4.9 Spectrum of UNDOPED UNCD with 0.3 μm thickness

4.5 Conclusion

As a conclusion, the table 4.9 shows the properties of the analyzed wafers. The stress values of wafers are classified based on different color. The green color shows the best stress values which can be used in CMUT fabrication. The yellow ones are located in the mid-range. But, the wafers with red colors are not desirable for usage in CMUT membrane.

Table 4.9 Properties of all diamond wafers

Sample ID	Diamond Type	Doping state	Diamond thickness	Base Wafer	Stress Value
1	MCD	UNDOPED	0.8	Si	+125
2	MCD	Br-DOPED	0.8	Si	+233
3	NCD	UNDOPED	1.7	Si/SiO ₂	-12.6
4	NCD	Br-DOPED	3.5	Si	+153
5	UNCD	UNDOPED	1.0	Si	-385
6	UNCD	Br-DOPED	1.0	Si/SiO ₂	364
7	UNCD	UNDOPED	0.3	Si	-178
8	UNCD	Br-DOPED	0.3	Si/SiO ₂	244

Raman spectroscopy is a very useful, non-destructive technique for the study of residual stress in diamond thin films with:

- Different crystal size
- Different doping state
- Different thickness size

CHAPTER 5

MICROFABRICATION of DIAMOND-BASED CMUT

In this thesis, the microfabrication of diamond-based CMUT is developed based on the direct bonding technique. Diamond is proposed as a membrane material. This chapter presents a step by step description of the process sequence followed to fabricate the CMUTs using only three masks. Most of the process steps of microfabrication were successfully performed in UNAM National Nanotechnology Research Center.

5.1 Cavity Patterning

Silicon wafers with a thickness of 1 μ m thermal SiO₂ is used in order to pattern the cavity. Thermally-oxidized silicon wafers are purchased from an outside vendor.

5.1.1 Photolithography of Silicon Wafers

Designed CAVITY mask for CMUT cells is transferred to a quartz mask in order to be used in photolithographic process. First, silicon wafer is held in hotplate at 150°C for 25 minutes in order to dehydrate the wafer. In the next step, the wafer is spread with HMDS in 4000 rpm spinning for 50 s. HMDS is used as an adhesion promoter for photoresist. AZ4533 is used as a photoresist material. Photoresist spreading is done in 4000 rpm for 50s; the coated photoresist has a thickness of 3.3 μ m. After photoresist covering, wafers are prebaked for 3 minutes and 20 seconds. The spinners and hotplates are shown in Figure 5.1.



(a)



(b)

Figure 5.1 (a) spinners, (b) hotplates

The cavity patterning is done by EVG620 mask aligner. UV light is used for wafer exposure with a constant dose of 60 mJ, and AZ400K: H₂O (1:4) developer is used for cell patterning for 106 seconds. The wafer's picture during the developing is shown in Figure 5.2.

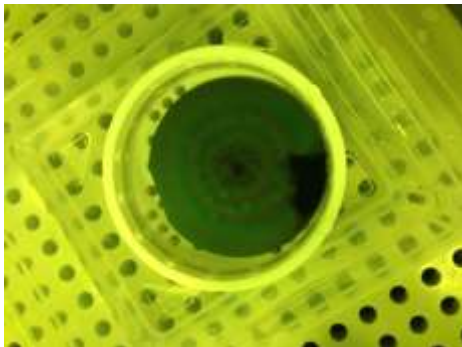


Figure 5.2 Cavity Patterned Wafer during developing

5.1.2 Wet and Dry Etching on Cavity Definition

In order to achieve a well defined cavity with a good depth control, reactive ion etch, RIE, is used. After 1 hour RIE oxide etch, the wafer is held in NANOPLAS for 2 hours in order to remove the photoresist residues. Finally, PIRHANA cleaning is necessary to clean all organic contaminants and photoresist residues that may build up on the wafer surface. In the PIRHANA cleaning, the first step is removal of all organic coatings in a strong oxidant, such as a 1:8 mixture of H₂O₂:H₂SO₄ in 140°C for 15 minutes. The PIRHANA system is shown in Figure 5.3.

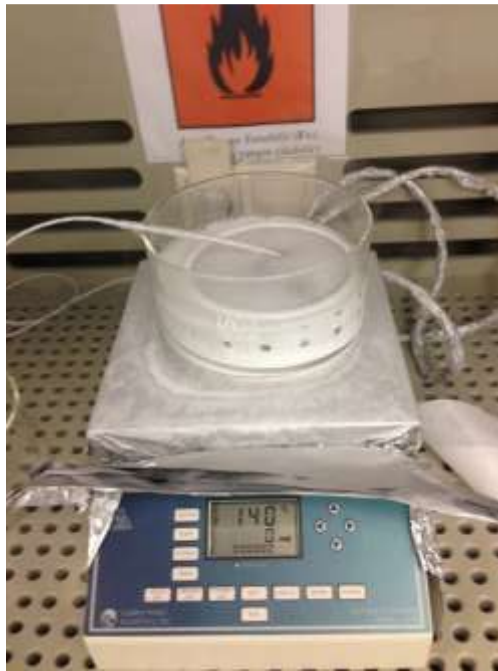


Figure 5.3 PIRHANA cleaning

Then the wafer is washed manually with DI water. Obtained hexagonal membrane cell structures after etching process are shown in Figure 5.4.

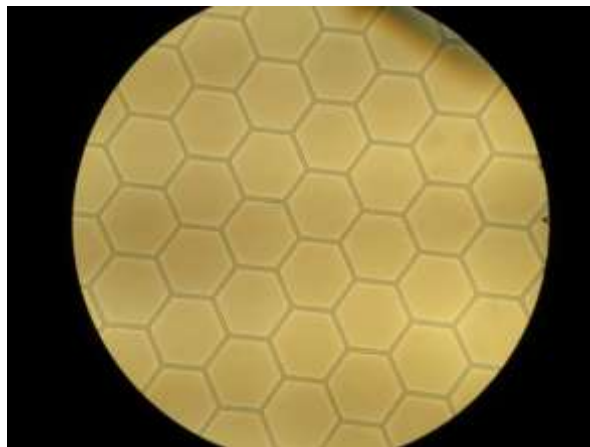


Figure 5.4 Microscope image of cavity pattern with 80um hexagons
(Central view, x20 lens)

5.1.3 UV Cleaning System

UV Cleaning is an indispensable technology to as it provides a simple and fast method of modifying and obtaining ultra-clean surfaces. Modification directly enhances the adhesion power of the treated surface, while cleaning gets rid of residual organic contaminants. Ultraviolet Ozone System is used to remove photoresist residues in 100°C for 31 minutes. The UV cleaning system is shown in Figure 5.5.

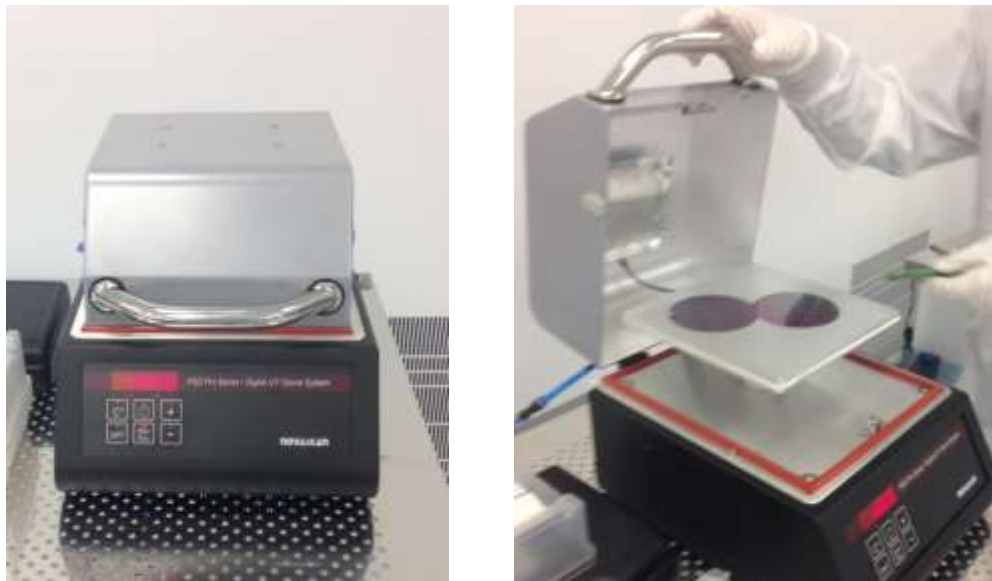


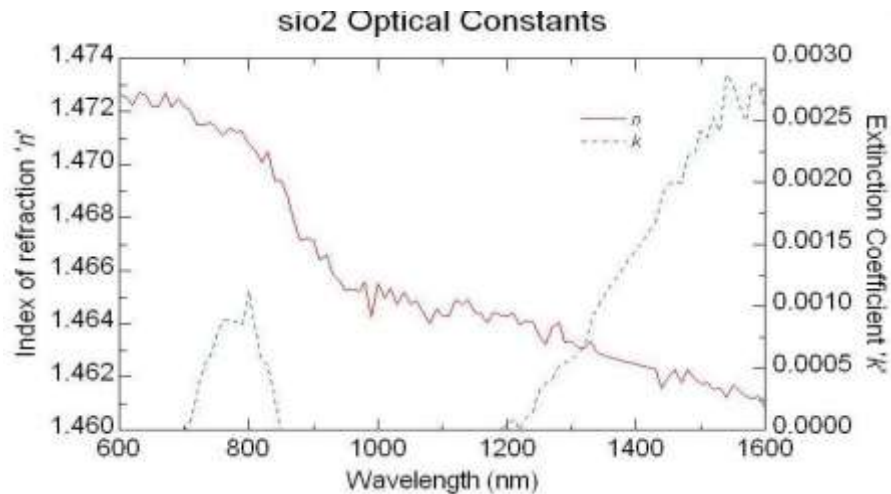
Figure 5.5 UV cleaning system

5.2 SiO₂ Deposition and CMP of Diamond Wafer for Wafer bonding

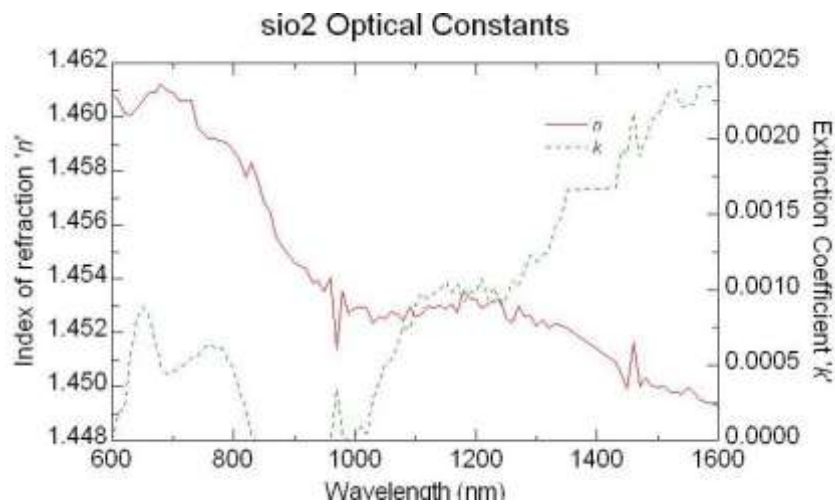
In order to have oxide on the diamond, the PECVD method is used. The required conditions for deposition of SiO₂ layer are keeping the wafers in furnace of 300 °C containing SiH₄+N₂O+He gases under 1 Torr pressure. The PECVD SiO₂ layer with a thickness of 500 nm is deposited on diamond wafers. In order to increase the quality of the coated SiO₂, RTA (Rapid Thermal Annealing) is used for annealing wafers. RTA takes out the gasses that have been trapped inside the coated oxide layer. The thickness and optical constants of the material are measured with V-Vase ellipsometer. Thickness measurements are dependent on the optical constants. The optical path length of light that traveled through the film is affected by the film thickness. The n and k values determine the light wave's velocity and refracted angle. Thus, both contribute to the delay between surface reflection and light traveling

through the film. Both n and k must be measured along with the thickness to get the correct results from an optical measurement.

The n and k values vary with different wavelengths and must be described at all wavelengths probed with the ellipsometer. The measurement is done in the range of 600-1600 wavelengths. After the measurement the thickness of the SiO_2 is found 547 nm. The Figure 5.6 shows the optical constants graphics before and after the RTA. As shown in graphics, there is a decrease in the n value as wanted.



(a)



(b)

Figure 5.6 (a) 'n' and 'k' constants graphics before RTA (b) 'n' and 'k' constants graphics after RTA

The surface roughness of SiO₂ layer value was not sufficient for proper direct bonding. In order to improve surface roughness, CMP (Chemical Mechanical Polishing) is performed.

5.3 Wafer Bonding

The most important step in CMUT fabrication is wafer bonding. Quality of wafer bonding usually determines the yield and robustness of CMUT devices. In this section, direct wafer bonding experiments have been demonstrated. Silicon-to-diamond with an interlayer of SiO₂, wafer bonding experiment has been performed. The two wafers must be cleaned and rinsed thoroughly to get a smooth and clean surface for the bonding process. Surfaces that are in contact with each other initially form weak physical forces. These physical forces are converted into strong chemical forces with high temperature annealing.

5.3.1 RCA Cleaning

RCA cleaning is necessary to clean all organic contaminants that may build up on the wafer surface. In the RCA cleaning, the first step is removal of all organic residues in a 5:1:1 mixture of H₂O: NH₄OH: H₂O₂ (“RCA1”) in 80°C for 15 minutes. Then ionic contaminants are removed with a 6:1:1 mixture of H₂O: HCL: H₂O₂ (“RCA2”) for 15 minutes in 80°C. Finally, the wafers are washed with water for 5 minutes. The RCA cleaning system is shown in Figure 5.7.



Figure 5.7 RCA cleaning system

5.3.2 Surface Wettability

Wetting is the ability of a liquid to maintain contact with a solid surface, resulting from intermolecular interactions when the two are brought together. The degree of wetting is determined by a force balance between adhesive and cohesive forces. Wettability is a crucial parameter in the wafer bonding. UV radiation modifies the wetting properties of the surface which becomes super-hydrophilic. The UV ozone cleaning system is used to increase the wettability of wafers. Both of the wafers, substrate and membrane wafers are activated for 21 minutes in 60 °C in air.

5.3.3 Wafer Bonding and High Temperature Annealing

The bond annealing is done in 300 °C or 450 °C for 5 hours. Fireplace glass is used to prepare required force of 100 N for the direct bonding of 4-inch wafers. Table 5.1 shows the properties of fireplace glass properties.

Table 5.1 Fireplace glass properties

Working Temperature	Thermal Shock Resistance	Specific Weight	Plate Size	Thickness
700°C	DTmax 700°C	2.55 gr/cm ³	200*200 mm	4mm

The Figure 5.8 shows the wafer bonding and annealing system used in this study.



Figure 5.8 Wafer bonding annealing system

Full wafer direct bonding was potentially done with pieces (area) layer transfers. The Figure 5.9 shows the layer transfer areas.



Figure 5.9 Wafer Bonding Results

5.4 Etching the Top Wafer

When the bonding process is completed, chemical etching of the whole silicon wafer of the diamond side is performed. To keep the bottom wafer out of harms way, it is held in wafer holder with backside and edge protection. The wafer holder is shown in Figure 5.10.

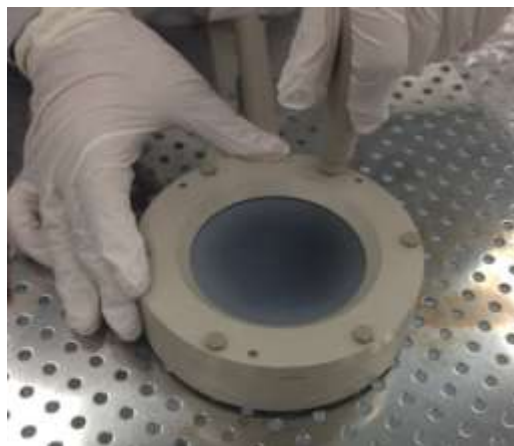


Figure 5.10 Wafer holder with backside and edge protection

The wafer is removed by TMAH at 98°C. TMAH is the most popular silicon anisotropic etchant. The TMAH etching temperatures are between 70-90 °C and typical concentrations are 5-25 wt% TMAH in water. (100) silicon etch rates generally increase with temperature and decrease with increasing TMAH concentration. Etched silicon (100) surface roughness decreases with increasing TMAH concentration, and smooth surfaces can be obtained with 20% TMAH solutions. (100) etch rates for 20 wt% solutions are shown in table 5.2.

Table 5.2 (100) etch rates according to temperature

Temperature	50 °C	80 °C	95 °C
Etch rate	4 μm/h	33 μm/h	80 μm/h

The TMAH process setup is shown in Figure 5.11.

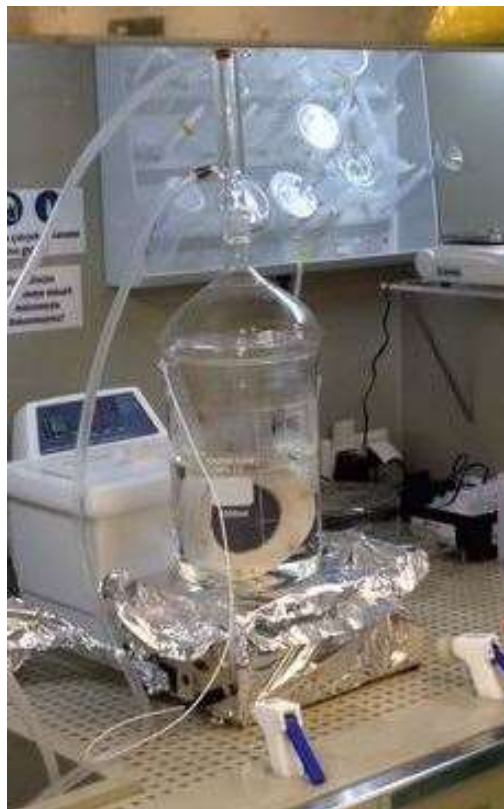


Figure 5.11 TMAH process setup

Figure 5.12 shows the wafer after TMAH process.

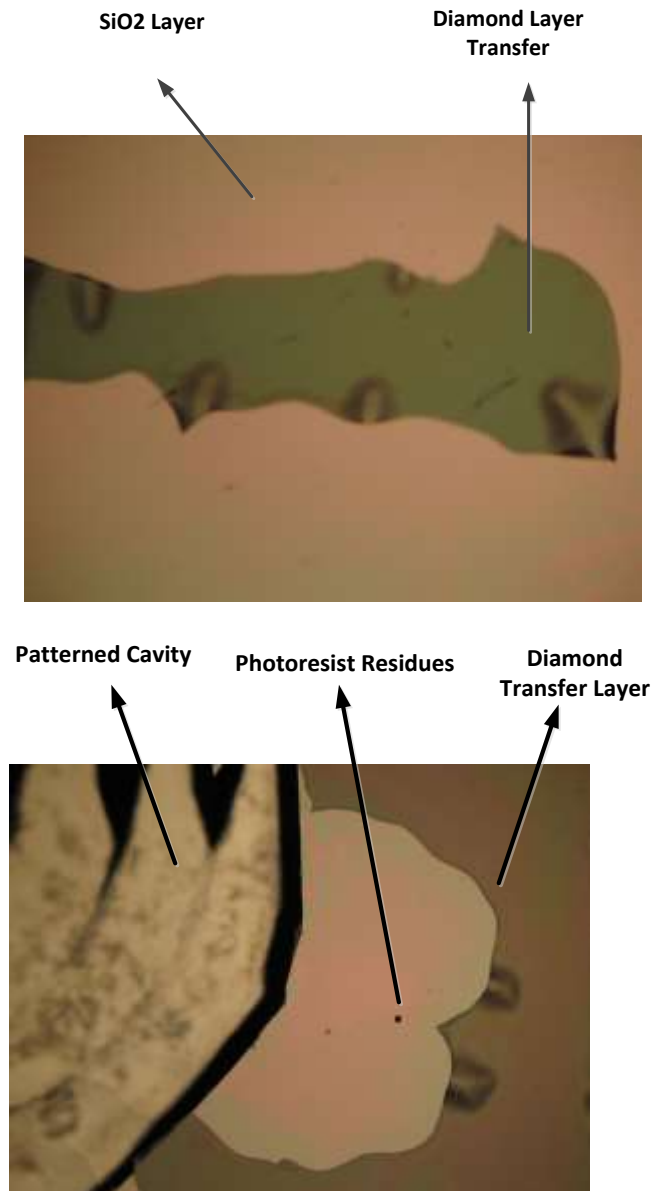


Figure 5.12 Microscope images of surface of wafer after TMAH process

Unfortunately, the bonding was partially successful due to the photoresist residues on the wafer surface after the lithography of the CAVITY mask. That resulted in the broken diamond membrane. Therefore, the further planned processing could not be continued over the processed wafer. Because of the limitations of wet cleaning (lack of megasonic and dump-rinse cleaning), the successful cleaning of the patterned wafer could not be achieved, and hence realization of the full process flow is left as is. The planned processing of the wafer is as follows:

5.5 MASK2: TOPLAYER

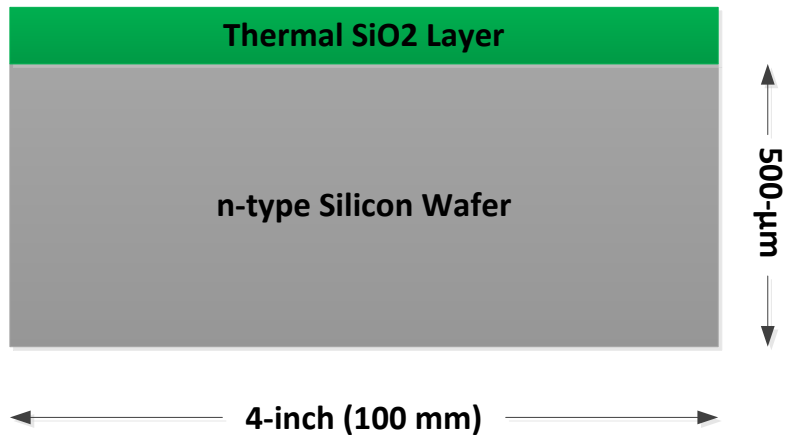
Cavities supplying the connection for the ground electrodes should be patterned. With the second masking process, metal regions for ground contact will be shaped. PECVD oxide layer will be deposited on to the diamond surface and patterned as a protection layer for diamond etching.

5.6 MASK3: METAL

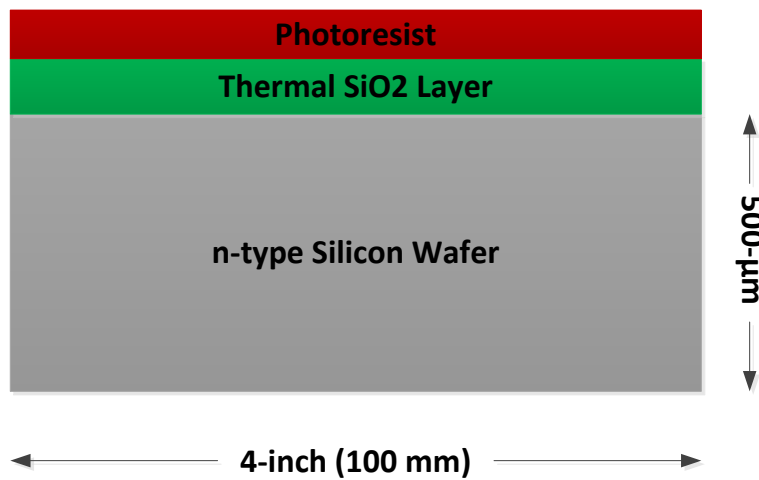
In this process step, tri-metal (Ti/Cu/Au) will be deposited using the Thermal Evaporator. Ti (30 nm) will be used for good adhesion of the metal on diamond. Cu (50 nm) will be used for diffusion barrier of the Au (500 nm) layer on top. After the metal deposition, it will be patterned with the third mask.

At the completion of this step, the CMUT will be realized.

5.7 Overview of Microfabrication steps of CMUTs with Diamond Membranes

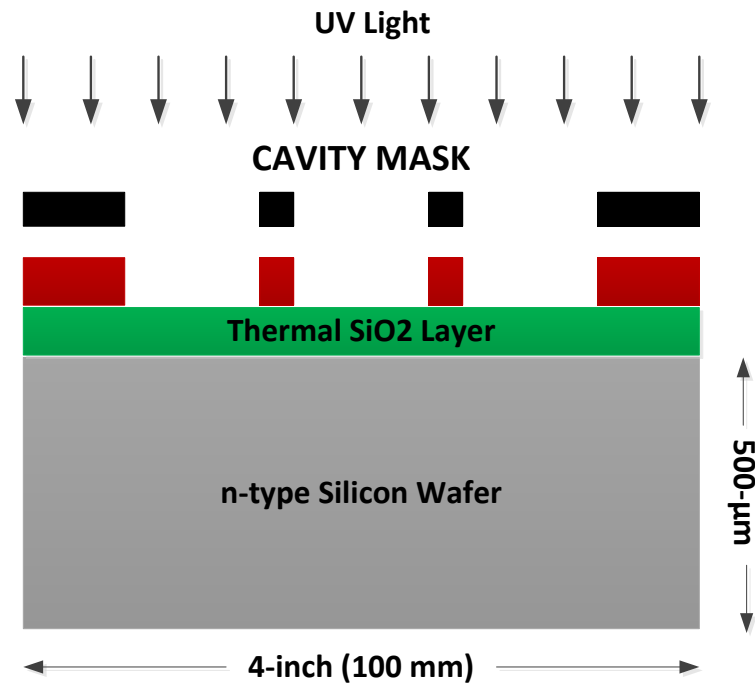


Step 1

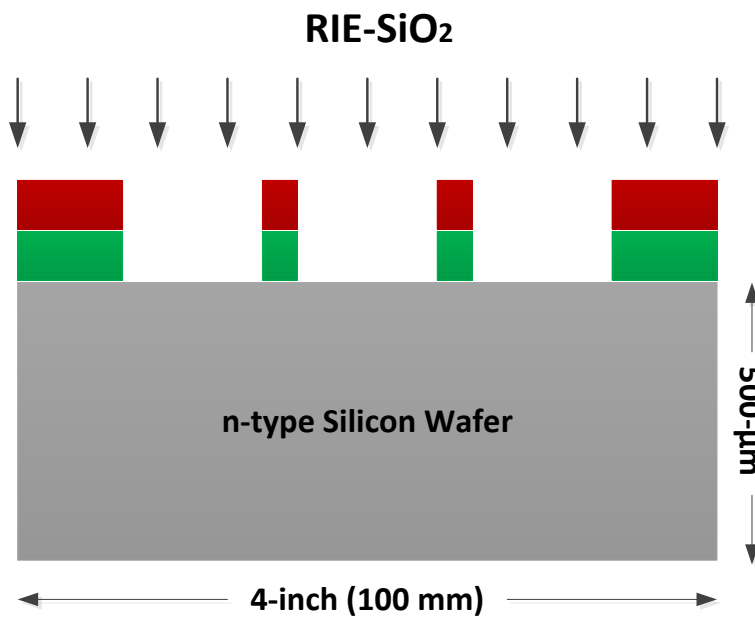


Step2

Figure 5.13: Process steps 1 to 2, Step 1: n-type silicon wafer with SiO₂ Layer, Step 2: Covering the wafer with photoresist

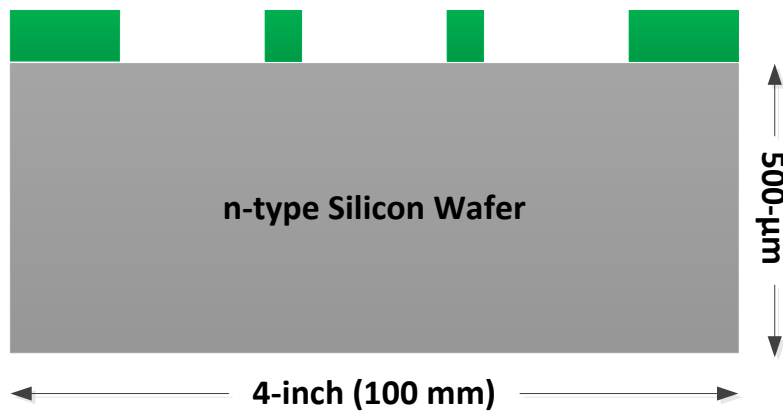


Step 3

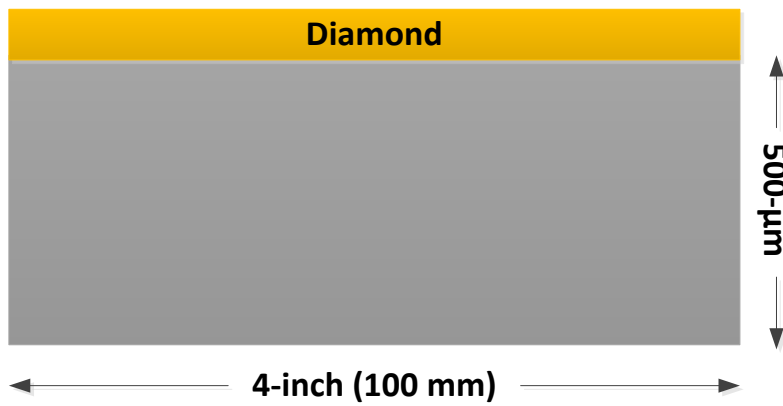


Step 4

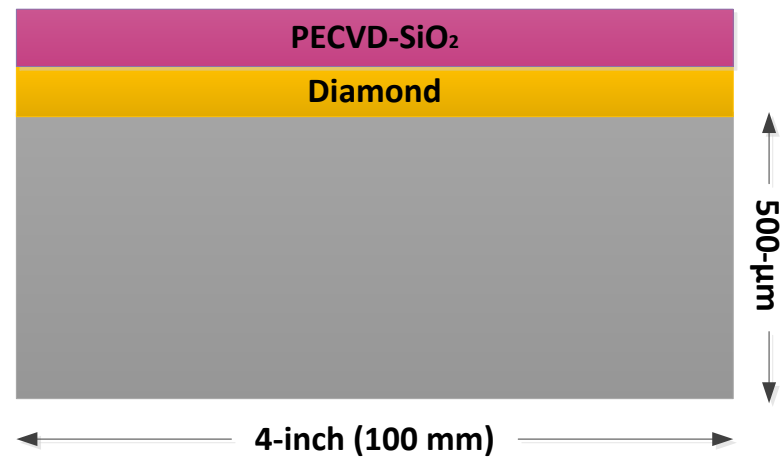
Figure 5.14 Process steps 3 to 4, Step 3: Photoresist patterning with cavity mask, Step 4: SiO₂ etching with RIE



Step 5

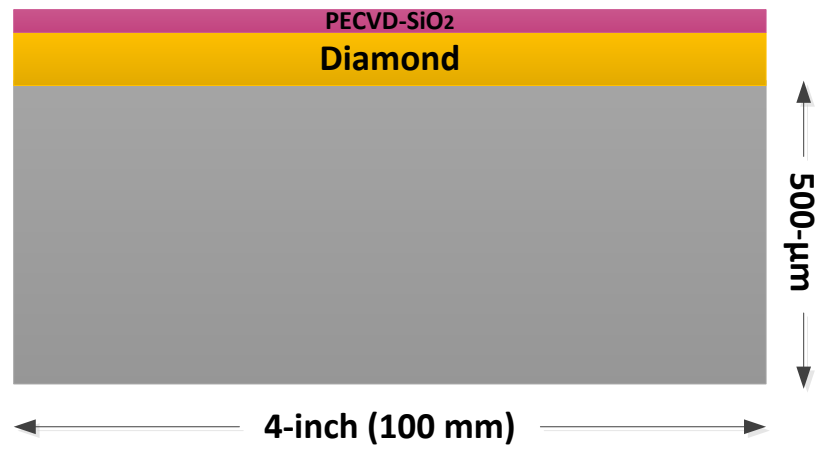


Step 6

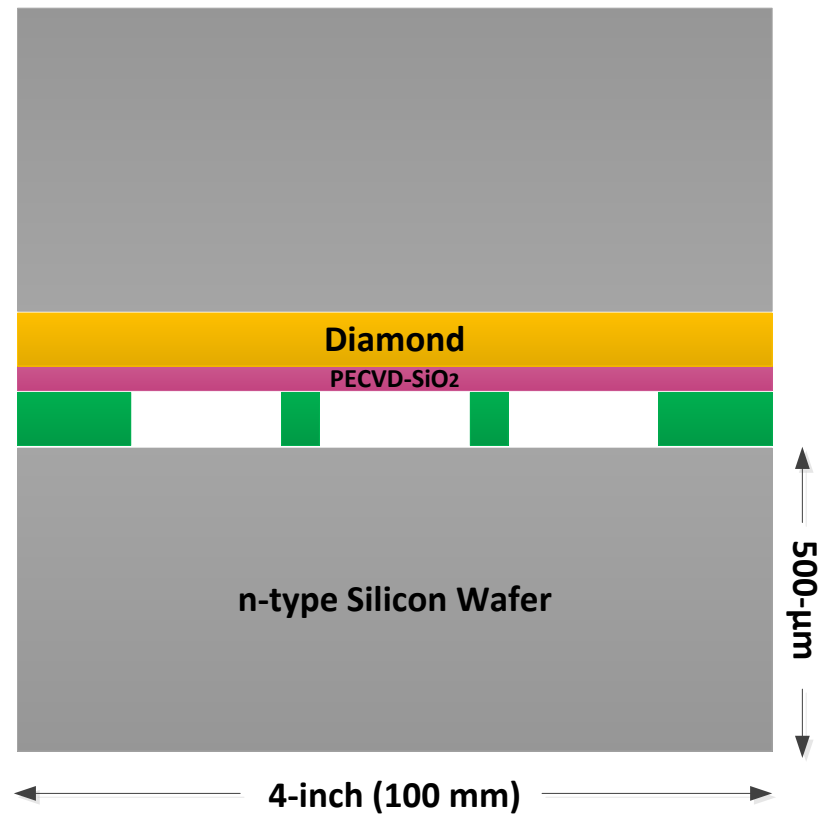


Step 7

Figure 5.15 Process steps 5 to 7, Step 5: Photoresist stripping with O₂ plasma, Step 6: Silicon wafer with diamond layer, Step 7: SiO₂ Deposition with PECVD

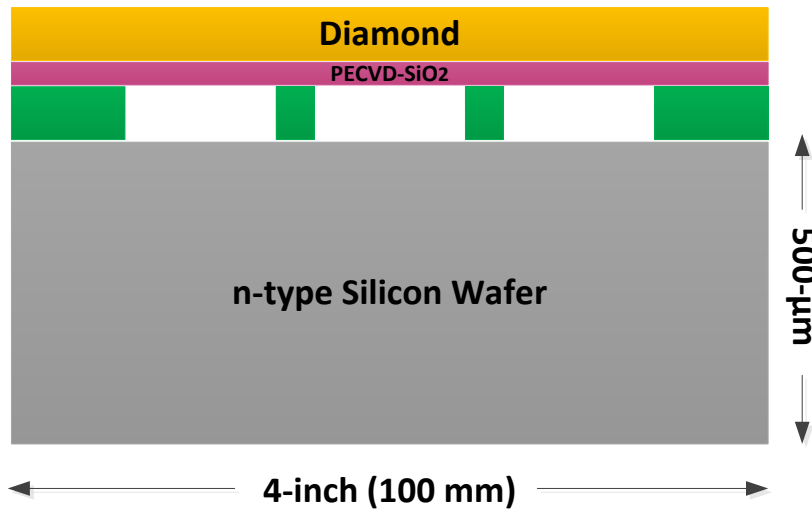


Step 8

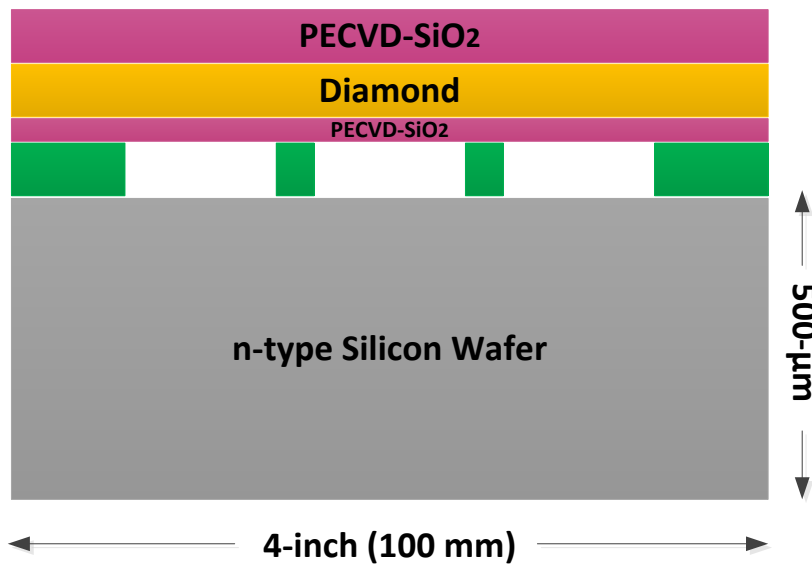


Step 9

Figure 5.16 Process steps 8 to 9, Step 8: Satisfy the surface roughness of PECVD-SiO₂ with CMP, Step 9: Direct bonding of wafers at 450°C.

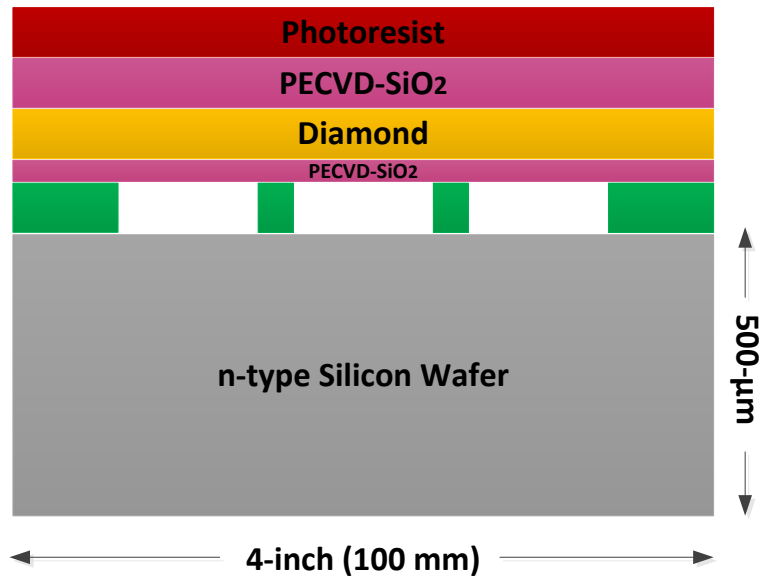


Step 10



Step 11

Figure 5.17 Process steps 10 to 11, Step 10: Total TMAH etching of 525 μ m silicon layer of top wafer, Step 11: PECVD SiO₂ covering of diamond surface

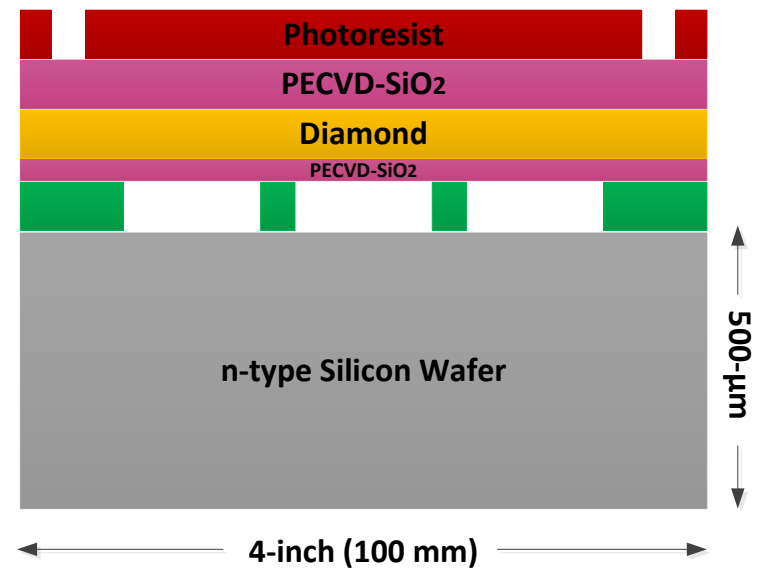


Step 12

UV-Light

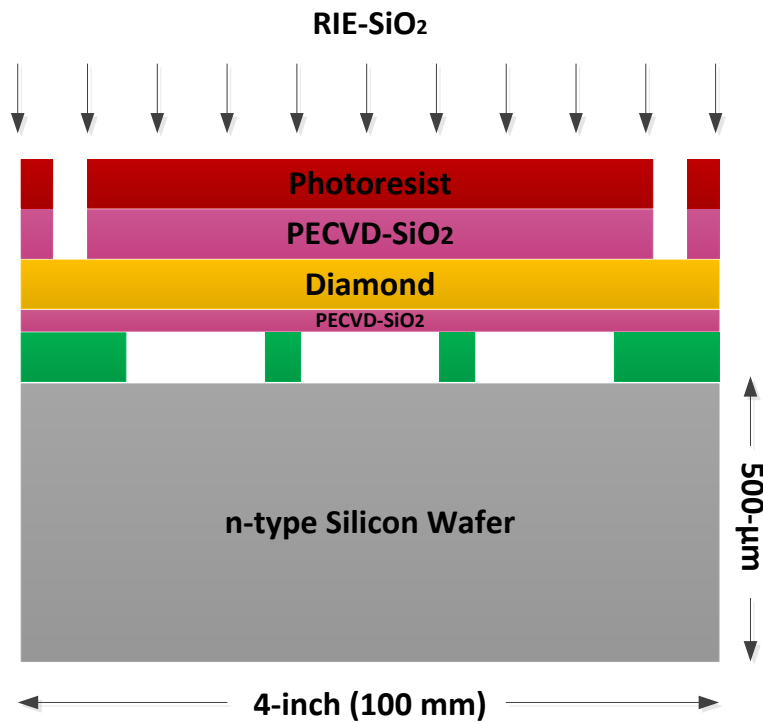


TOPLAYER Mask

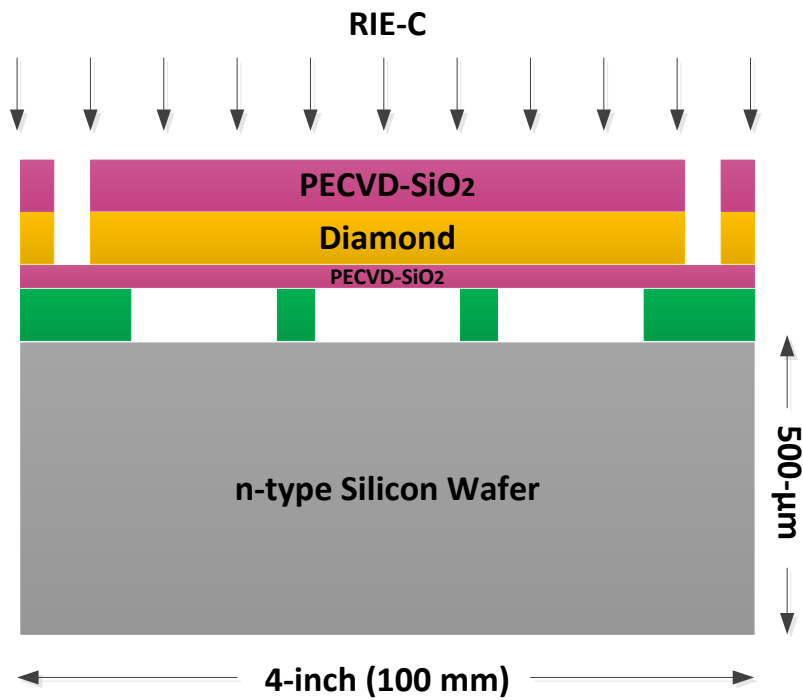


Step 13

Figure 5.18: Process steps 12 to 13, Step 12: Photoresist covering, Step 13: Photoresist patterning with TOPLAYER mask

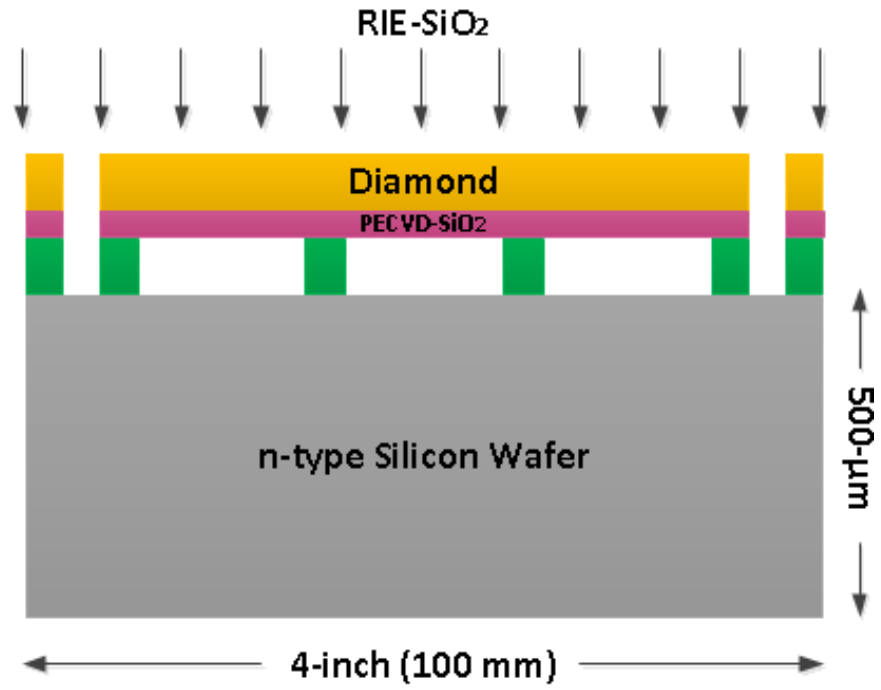


Step 14

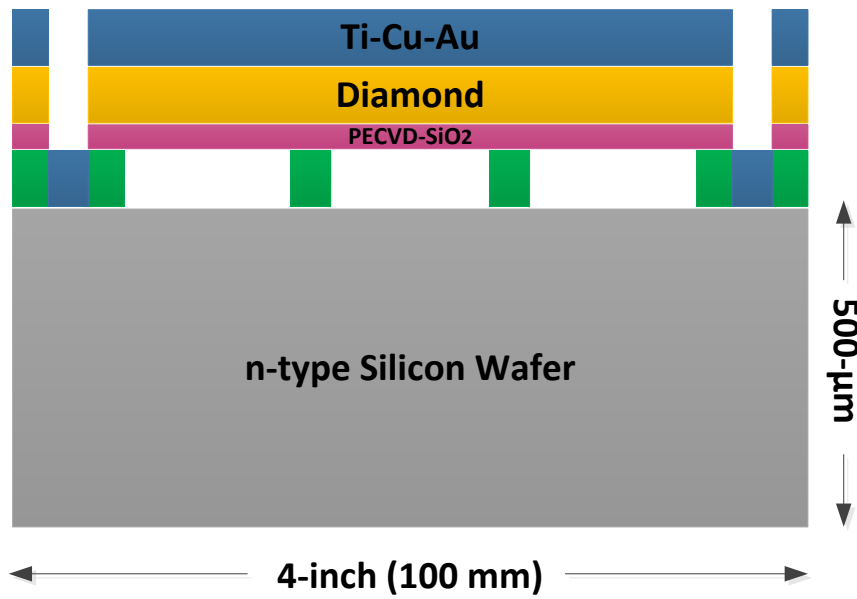


Step 15

Figure 5.19 Process steps 14 to 15, Step 14: SiO₂ etching with RIE, Step 15: Diamond etching with RIE and photoresist stripping

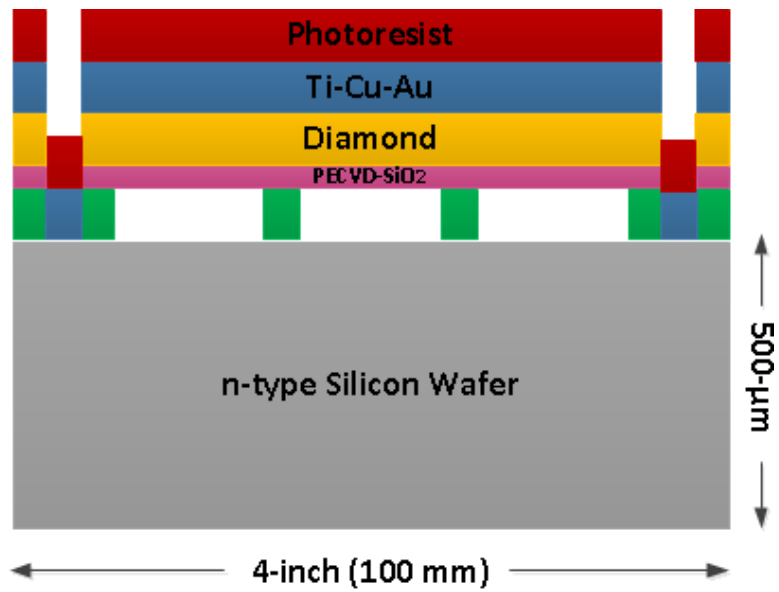


Step 16

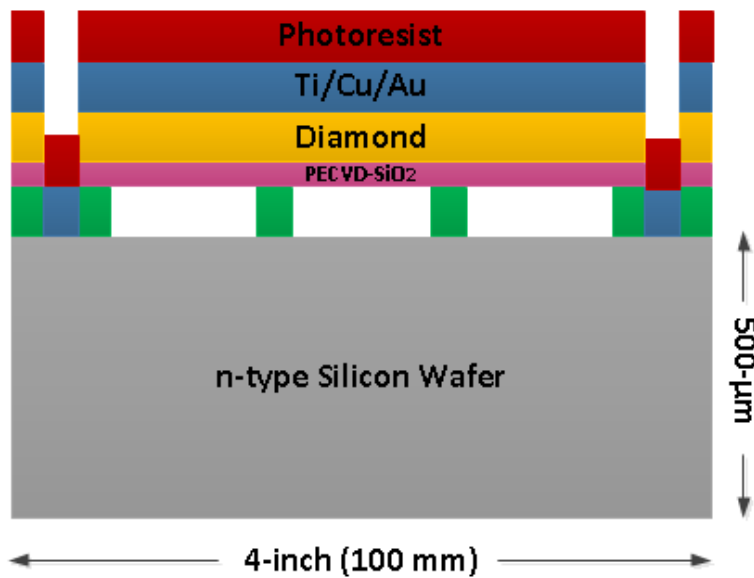
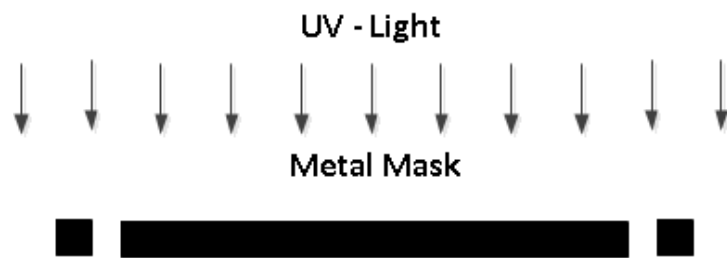


Step 17

Figure 5.20 Process steps 16 to 17, Step 16: SiO₂ etching with RIE, Step 17: Metallization



Step 18



Step 19

Figure 5.21 Process steps 18 to 19, Step 18: Photoresist Covering, Step 19: Patterning Photoresist with Metal Mask

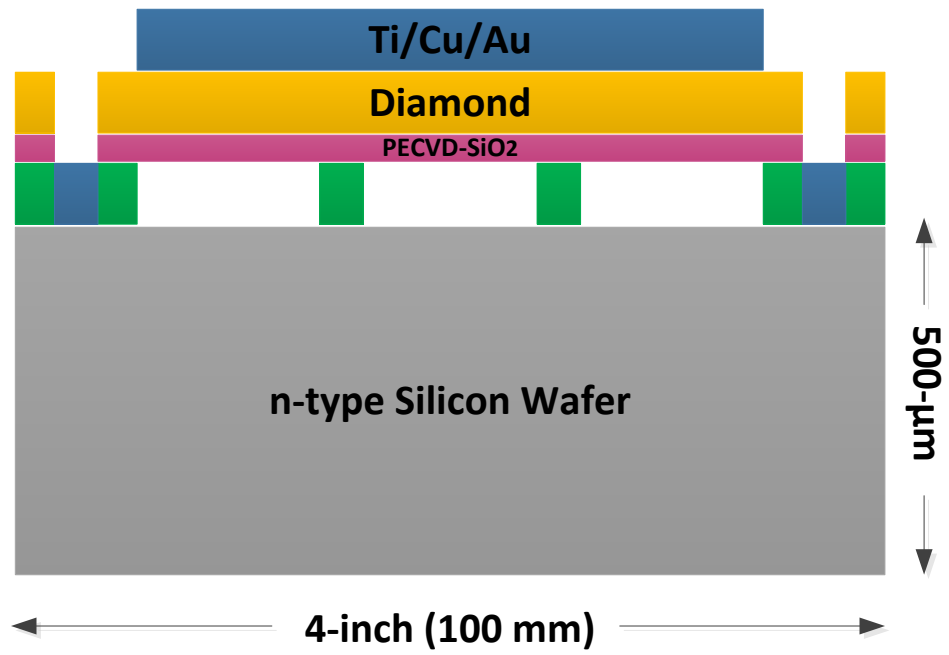


Figure 5.22 Process Step 20: Metal etches with chemicals and photoresist stripping with O₂ plasma

CHAPTER 6

Conclusions and Future Work

In this thesis, a novel concentric annular CMUT design has been fully designed. All design parameters are determined based on the analytical expressions based on CMUT theory. Each CMUT design consists of 4 concentric disc-shaped elements, having equal membrane areas. Each element features hexagonal CMUT cells having side lengths of 50 μm up to 80 μm . The CMUT design features fully-metallized membranes for robust operation. The novel CMUT design presented in this thesis is a state-of-the-art design based on microfabrication using direct wafer bonding technology. A complete microfabrication process flow has been developed for the realization of the CMUT design.

- 1) Diamond coating on the silicon wafer has been characterized in terms of residual stress via Raman Spectroscopy measurements, and viability as a membrane material has been shown.
- 2) A complete microfabrication process flow has been developed. An interlayer of PECVD-SiO₂ is used on the diamond layer. An RTA is used to improve the quality of the oxide layer, which is characterized thoroughly using a V-VASE ellipsometer.
- 3) A surface activation for direct wafer bonding is developed based on a combination of UV/Ozone treatment followed by O₂-plasma-activation using RIE. A successful bonding is achieved on two flat wafer surfaces.
- 4) A TMAH etching system of silicon wafer using a special wafer holder with backside and etch protection is used to fully etch the silicon bulk wafer.

Due to lack of some essential cleanroom capabilities, a fully functional prototype could not be realized in our work. However, it is straightforward to microfabricate the CMUT based on the outcome of this thesis in the presence of a cleanroom having the essential equipment and setup.

In the future work, a fully functional CMUT microfabrication is planned using a megasonic cleaning system to properly clean the photoresist residues after the first lithography step. We believe that megasonic is essential for the proper removal of the small particles impeding the direct bonding process.

REFERENCES

- [1] An information portal for the MEMS and Nanotechnology community, <https://www.memsnet.org>
- [2] B. A. J. Angelsen, Waves, signals and signal processing in medical ultrasonics. Trondheim: Department of Physiology and Biomedical Engineering, Norwegian University of Science and Technology, 1996.
- [3] Piezotechnology, http://www.piceramic.com/piezo_transducer_tutorial.php
- [4] D. Spoliansky, I. Ladabaum, and B.T. Khuri-Yakub, "Micromachined ultrasonic air transducers (MUTs)," *Microelectron. Eng.*, vol. 30, pp. 535 - 538, 1996.
- [5] Khuri-Yakub, Ultrasonic Group, Stanford University, <http://www-kyg.stanford.edu/khuriyakub/opencms/en/home/index.html>
- [6] M. I. Haller and B. T. Khuri-Yakub, "A surface micromachined electrostatic ultrasonic air transducer," in *Proc. IEEE Ultrason. Symp.* 1994, pp. 1241-1244.
- [7] H.T. Soh, I. Ladabaum, A. Atalar, C.F. Quate, and B.T. Khuri-Yakub, "Silicon micromachined ultrasonic immersion transducers," *Appl. Phys. Lett.*, vol. 69, pp. 3674 - 3676, 1996.
- [8] I. Ladabaum, X.C. Jin, and B.T. Khuri-Yakub, "Miniature drumheads: microfabricated ultrasonic transducers," *Ultrasonics*, vol. 36, pp. 25 - 29, Feb. 1998.
- [9] I. Ladabaum, X.C. Jin, H.T. Soh, A. Atalar, and B.T. Khuri-Yakub, "Surface micromachined capacitive ultrasonic transducers," *IEEE T. Ultrason. Ferr.* vol.45, no.3, pp.678-690, 1998.

- [10] Y. Roh, and B.T. Khuri-Yakub, "Finite element analysis of underwater capacitor micromachined ultrasonic transducers," *IEEE T. Ultrason. Ferr.* vol.49, no.3, pp. 293-298, 2002.
- [11] G.G. Yaralioglu, A.S. Ergun, B. Bayram, E. Haeggstrom, and B.T. Khuri-Yakub, "Calculation and measurement of electromechanical coupling coefficient of capacitive micromachined ultrasonic transducers," *IEEE T. Ultrason. Ferr.* vol. 50, no. 4, pp. 449-456, 2003.
- [12] B. Bayram, E. Haeggstrom, G.G. Yaralioglu, and B.T. Khuri-Yakub, "A new regime for operating capacitive micromachined ultrasonic transducers," *IEEE T. Ultrason. Ferr.* vol. 50, no. 9, pp. 1184- 1190, 2003.
- [13] M.H. Badi, G.G. Yaralioglu, A.S. Ergun, S.T. Hansen, E.J. Wong, and B.T. Khuri- Yakub, "Capacitive micromachined ultrasonic Lamb wave transducers using rectangular membranes," *Ultrasonics*, " *IEEE T. Ultrason. Ferr.* vol. 50, no. 9, pp. 1191- 1203, 2003.
- [14] B. Bayram, O. Oralkan, A.S. Ergun, E. Haeggstrom, G.G. Yaralioglu, and B.T. Khuri- Yakub, "Capacitive micromachined ultrasonic transducer design for high power transmission," *IEEE T. Ultrason. Ferr.* vol. 52, no. 2, pp. 326- 339, 2005.
- [15] B. Bayram, G.G. Yaralioglu, M. Kupnik, A.S. Ergun, O. Oralkan, A. Nikoozadeh, and B.T. Khuri-Yakub, "Dynamic analysis of capacitive micromachined ultrasonic transducers," *Ultrasonics*, *IEEE T. Ultrason. Ferr.* vol. 52, no. 12, pp. 2270- 2275, 2005.
- [16] O. Oralkan, B. Bayram, G.G. Yaralioglu, A.S. Ergun, M. Kupnik, D.T. Yeh, I.O.Wygant and B.T. Khuri-Yakub, "Experimental characterization of collapse-mode CMUT operation," " *IEEE T. Ultrason. Ferr.* vol. 53, no. 8, pp. 1513- 1523, 2006.
- [17] B. Bayram, M. Kupnik, G. G. Yaralioglu, O. Oralkan, A. S. Ergun, D. Lin, S. H. Wong, and B. T. Khuri-Yakub, "Finite element modeling and experimental characterization of crosstalk in 1-D CMUT arrays," *IEEE T. Ultrason. Ferr.* vol. 54, no. 2, pp. 418- 430, 2007.

- [18] S. H. Wong, M. Kupnik, X. Zhuang, D.-S. Lin, K. Butts-Pauly, and B. T. Khuri-Yakub, "Evaluation of Wafer Bonded CMUTs with Rectangular Membranes Featuring High Fill Factor," *IEEE T. Ultrason. Ferr.*, vol. 55, no. 9, pp. 2053-2065, 2008.
- [19] Y. Huang, X. Zhuang, E. O. Hæggestrom, A. S. Ergun, C.-H. Cheng, and B. T. Khuri-Yakub, "Capacitive micromachined ultrasonic transducers with piston-shaped membranes: Fabrication and experimental characterization," *IEEE T. Ultrason. Ferr.* vol. 56, no. 1, pp. 136-145, 2009.
- [20] K. K. Park, Ö. Oralkan, and B. T. Khuri-Yakub, "A Comparison Between Conventional and Collapse-Mode Capacitive Micromachined Ultrasonic Transducers in 10-MHz 1-D Arrays" *IEEE T. Ultrason. Ferr.* vol. 60, no. 6, pp. 1245-1255, 2013.
- [21] A. S. Ergun, G. G. Yaraliogly, and B. T. Khuri-Yakub, "Capacitive micromachined ultrasonic transducers: Theory and technology" *Journal of aerospace engineering*, vol. 16, no. 2, 1-apr-2003.
- [22] A.S. Ergun, Y. Huang, X. Zhuang, O. Oralkan, G.G. Yarahoglu, and B.T. Khuri-Yakub, "Capacitive micromachined ultrasonic transducers: fabrication technology," *IEEE T. Ultrason. Ferr.* vol. 52, no. 12, pp. 2242- 2258, 2005.
- [23] Y. Huang, A.S. Ergun, E. Haeggstrom, M.H. Badi, and B.T. Khuri-Yakub, "Fabricating capacitive micromachined ultrasonic transducers with wafer-bonding technology," *J. Microelectromech. S.* vol. 12, no. 2, pp. 128- 137, 2003.
- [24] X.C. Jin, I. Ladabaum, and B.T. Khuri-Yakub, "The microfabrication of capacitive ultrasonic transducers," *J. Microelectromech. S.*, vol.7, no.3, pp.295-302, 1998.
- [25] X.C. Jin, I. Ladabaum, F.L. Degertekin, S. Calmes, and B.T. Khuri-Yakub, "Fabrication and characterization of surface micromachined capacitive ultrasonic immersion transducers," *J. Microelectromech. S.*, vol.8, no.1, pp.100-114, 1999.
- [26] S. Vaithilingam, T.-J. Ma, Y. Furukawa, I. O. Wygant, X. Zhuang, A. de la Zerda, Ö. Oralkan, A. Kamaya, S. S. Gambhir, R. B. Jeffrey Jr., and B.T.

- Khuri-Yakub, , "Three-dimensional photoacoustic imaging using a two-dimensional CMUT array,," *Ultrasonics, Ferroelectrics and Frequency Control*, IEEE Transactions on, vol. 56, no. 11, pp. 2411-19, , Nov. 2009.
- [27] S. Vaithilingam, T.-J. Ma, Y. Furukawa, I. O. Wygant, X. Zhuang, A. de la Zerda, Ö. Oralkan, A. Kamaya, S. S. Gambhir, R. B. Jeffrey Jr., and B.T. Khuri-Yakub, , "Three-dimensional photoacoustic imaging using a two-dimensional CMUT array,," *Ultrasonics, Ferroelectrics and Frequency Control*, IEEE Transactions on, vol. 56, no. 11, pp. 2411-19, , Nov. 2009.
- [28] Y. Huang, E.O. Haeggstrom, X. Zhuang, A.S. Ergun, and B.T. Khuri-Yakub, "A solution to the charging problems in capacitive micromachined ultrasonic transducers," *IEEE T. Ultrason. Ferr.*, Vol. 52, no.4, pp. 578- 580 , 2005.
- [29] K. K. Park, H. Lee, M. Kupnik, and B. T. Khuri-Yakub, "Fabrication of capacitive micromachined ultrasonic transducers via local oxidation and direct wafer bonding," *Microelectromechanical Systems, Journal of*, vol. 20, no. 2, pp. 95-103, Feb. 2011.
- [30] B. Bayram, "Diamond-based capacitive micromachined ultrasonic transducers," *Diam. Relat. Mater.* vol. 22, no. 2, pp. 6-11, Feb. 2012.
- [31] M. S. Salim, M. F. Abd. Malek, R. B. W. Heng, K. M. Juni, N. Sabri, "Capacitive Micromachined Ultrasonic Transducers: Technology and Application" *Medical Ultrasound*, vol. 20, Issue 1 , pp. 8-31, March 2012
- [32] H. K. Oguz, S. Olcun, M. N. Senlik, A. Atalar, H. Koymen, "Nonlinear modeling of an immersed transmitting CMUT for harmonic balance analysis," *IEEE T. Ultrason. Ferr.* vol. 57, no. 2, pp. 438-447, Feb. 2010.
- [33] H. Koymen, A. Atalar, E. Aydoglu, C. Kocabas, H. K. Oguz, S. Olcun, A. Ozgurluk, A. Unlugedik, " An improved lumped element nonlinear circuit model for a circular CMUT cell", *IEEE T. Ultrason. Ferr.* vol. 59, no. 8, pp. 1791-1799, Aug. 2012.

- [34] E. Aydogdu, A. Ozgurluk, A. Atalar, H. Koymen, “ Parametric nonlinear lumped element model for circular CMUT’s in collapsed mode”, IEEE T. Ultrason. Ferr. vol. 61, no. 1, pp. 173-181, Jan. 2014.

